Light Water Reactor Sustainability Program

Evaluation of the stress and fluence dependence of irradiation assisted stress corrosion crack initiation in high fluence austenitic stainless steels under pressurized water reactor relevant conditions

September 2020

U.S. Department of Energy

Office of Nuclear Energy

Evaluation of the stress and fluence dependence of irradiation assisted stress corrosion crack initiation in high fluence austenitic stainless steels under pressurized water reactor relevant conditions

Gary S. Was
Donghai Du

September 2020

SUMMARY

The program consists of two major tasks; determination of the irradiation assisted stress corrosion cracking (IASCC) susceptibility of solution annealed (SA) 304 and cold-worked (CW) 316 stainless steel (SS) in PWR primary water environment. This was done using two principle test methods; the constant extension rate tests (CERT) to determine the stress-strain and fracture behaviors using tensile bars, and a four-point bend test to determine the stress to crack initiation and the microstructural features responsible for it. CW316 SS samples were irradiated to dpa levels of 46.9, 67.4 and 125.4 dpa in the BOR-60 reactor at RIAR, Russia, and SA304 SS samples were irradiated to dpa levels of 5.4, 69, 95 and 125.4 dpa. To date, all conditions of SA304 and CW316 have been tested using CERT and four-point bend experiments.

KEY FINDINGS

- CERT studies using a single strain method on neutron irradiated CW316 SS showed no dependence of IASCC on dose in the range of 46.9-125.4 dpa when measured by %Intergranular (IG) on the fracture surface.
- SA304 SS samples showed a slight but continuous increase in IASCC susceptibility with dose from 5.4 dpa to 125.4 dpa.
- The mode of straining (interrupted vs. single strain or varying strain rates) had a significant influence on the resulting %IG of the fracture surface.
- The effect of strain mode on %IG in 316 is understood by normalizing the %IG to the exposure time after yielding. The %IG exhibited an inverse relationship with the time after yielding irrespective of the strain mode and dose of the sample.
- In four-point bend tests, cracks formed at stresses as low as 45% of the irradiated yield stress in CW316 SS and 60% of the irradiated yield stress in SA304 SS.
- Cracks always nucleated at the grain boundary where at least one adjacent grain exhibited heavy localized deformation (slip lines or twins), or at triple junction where the local stress was also large.
- Grain boundary (GB) oxidization and dislocation channels intersecting the oxidized GB appeared before crack initiation, which are believed a precursor state for crack initiation.
- The number of cracked boundaries increased with stress and nearly all the crack trace inclination angles were larger than 60º indicating that the normal stress is driving crack initiation
- As the stress increased, small cracks grew into large cracks by coalescence.
- The crack initiation threshold stress in the simulated PWR primary water environment is about 40% of irradiated yield strength.

ACKNOWLEDGEMENT

Contents

FIGURES

TABLES

ACRONYMS

ASTM	American Society of Testing and Materials
BWR	boiling water reactor
BSE	backscattered electron
CERT	constant extension rate tensile
CW	cold-work
DC	dislocation channel
DO	dissolved oxygen
EBSD	electron back-scattered diffraction
EDX	energy-dispersive X-ray spectroscopy
EDM	electron discharge machining
EELS	electron energy loss spectroscopy
EPRI	Electric Power Research Institute
FWHM	full width at half maximum
HR	high resolution
GB	grain boundary
IASCC	irradiation assisted stress corrosion cracking
IG	intergranular
IMTL	Irradiated Materials Testing Laboratory
LAMDA	Low Activation Materials Development and Analysis
LD	localized deformation
LVDT	linear variable differential transformer
LWR	light water reactors
ORNL	Oak Ridge National Laboratory
PWR	pressurized water reactor
RIS	radiation induced segregation
SA	solution anneal
SEM	scanning electron microscope
SS	stainless steel
TEM	transmission electron microscope
TJ	triple junction
UM	University of Michigan
YS	yield strength

Evaluation of the stress and fluence dependence of irradiation assisted stress corrosion crack initiation in high fluence austenitic stainless steels under pressurized water reactor relevant conditions

1. INTRODUCTION

This program addresses the cause of IASCC in LWR core internals in PWR primary water chemistry, intending to provide a foundation for material performance predicting models and mitigation strategies by determining the key factors controlling the process. Irradiation assisted stress corrosion cracking (IASCC) continues to cause failures in key components of both PWRs and BWRs in the US and international reactor fleets. Identified in the 1960s, IASCC is generic in that all water reactors have exhibited susceptibility over a wide range of alloys and components. The problem will gain increasing importance in the coming years due to two factors; 1) the life extension to 60 years and perhaps to 80 years for the existing reactor fleet, and 2) the introduction of advanced reactors that will be subjected to the same types of environments.

Between the years 2000 and 2010, tensile and compact tension specimens as well as transmission electron microscope (TEM) discs of multiple alloys were irradiated in the BOR-60 fast reactor in RIAR, Russia as part of the framework of BORIS (BOR-60 Internal Study) irradiation experiments [1, 2]. The typical dose range was 5–20 dpa, but several capsules reached or exceeded 100 dpa. Irradiated specimens were involved in multiple programs including the Cooperative IASCC Research program [2]. Under certain circumstances, irradiated materials and untested specimens were made available to research teams working in the radiation materials field. Types 308, 304, and 316 stainless steel specimens with various dpa levels were among the samples irradiated in BOR-60.

During FY2016–2017, a collaborative effort was launched to transport several high- and very-high-dose specimens (up to 125 dpa) from Dimitrovgrad, Russia, to Halden, Norway, and after that to Oak Ridge National Laboratory (ORNL) in Oak Ridge, Tennessee. Much of the effort involved acquiring the proper license(s) and documenting that irradiated materials were appropriately prepared for shipment. The irradiated materials arrived in Halden, Norway, on August 23, 2016. After that, new activity calculations, inventory, additional packaging, documentation, and licensing efforts were pursued. The materials were shipped from the Halden reactor to ORNL in early 2018.

In March 2018, 13 tensile specimens were delivered to the Irradiated Materials Examination and Testing hot cell facility at ORNL. The internal holder with specimens was extracted and examined, revealing no transportation-related issues. Finally, specimens were unloaded and underwent individual examination and inventory and were made available to this project.

The focus of this program is on the determination of IASCC susceptibility of highly irradiated 300-series alloys in simulated PWR primary water with various damage levels, the minimum stress to cause crack initiation, and the correlation to microstructure features, and identification of potential mitigation strategies. Of special interest are the dose dependence of crack initiation to very high dpa, the nature of the initiation site, and the role of localized deformation in crack initiation of highly irradiated stainless steel.

The outcome of this program will provide a firmer understanding of parameters and microstructures governing IASCC and key elements that need to be included in a predictive model of the initiation of IASCC cracks that can be used to develop mitigation techniques.

The IASCC susceptibility of highly neutron irradiated stainless steel with a dose up to 125 dpa in the PWR environment is still unknown. To evaluate the IASCC susceptibility of these materials, a constant extension rate tensile test technique was used to reveal the change of fracture behavior and mechanical property with dpa. The role of stress and microstructural features on the crack initiation in austenitic stainless steels in the PWR environment under the presence of radiation is also not properly understood. To address this issue, the four-point bend test was used to identify the critical stress to induce crack imitation and the microstructure features that correlate with crack initiation.

2.   EXPERIMENT

2.1   Materials and Specimens

2.1.1   Materials

The alloys investigated in this study are ~15% cold-worked (CW) 316 stainless steel (SS) and solution annealed (SA) 304 SS. The chemical compositions of the alloys in this program (in wt.%) are given in Table 1. The irradiations were performed in BOR-60 fast reactor at a temperature of 320°C with a neutron flux of ~1.8×10^{15} n/cm^{2}s (E>0.1 MeV), which corresponds to a damage rate of 9.4×10^{-7} dpa/s using the NRT model [1]. In the table, the suffix E stands for cold-worked material, and the suffix H represents the traditional solution annealed condition.

Table 1. Chemical compositions (wt.%) of the 300-series stainless steels.

Alloy/heat	C	S	P	Si	Mn	Ni	Cr	Mo	Cu	Co	Nb-Ta	B (ppm)	O (ppm)	N (ppm)
316-1 E/EDF	0.054	0.022	0.027	0.68	1.12	10.6	16.6	2.25	0.24	0.12	0.01	5	41	230
304-1 H/Creusot-Loire	0.022	0.0007	0.032	0.38	1.79	9.88	18.61	-	0.25	0.064	-	9	-	610

2.1.2   Sample preparation

Two pieces of material sliced from a tensile bar head using Electron Discharge Machining (EDM) were used to prepare four-point bend samples. The position where the slices were made and the dimensions of the four-point bend sample are shown in Figure 1. The remaining material was used to prepare transmission electron microscopy (TEM) samples. Rectangular samples with 1 mm thickness were made after EDM cutting. A Buehler Mini-met 1000™ sample grinding and polishing tool performed sample thinning to a target thickness of 800 μm using 120, 180, and 340 grit SiC grinding paper on each side to achieve a uniform thickness (final thickness variations were less than 10 μm). One side of the sample was then polished with a nylon pad containing 3 μm polishing media in the Mini-met™ and subsequently electrochemically polished in a Struers LectroPol-5™ system in four steps. One electrochemical polishing step was applied for 15 s at a potential of 30 V at 20 °C in a commercially available Struers A2 solution (60% perchloric acid). The final dimensions of the four-point bend sample are shown in Figure 1b. The ID, dose, and thickness of four-point bend samples tested in this study are given in Table 2. The thickness of sample

B101-B1 is not uniform, increasing from 720 to 800 μm along the short axis. There are also samples thicker than the target value (800 μm), such as B35-B1, A98-1-2, A96-1-2, and A32-1-1.

(a)   (b)
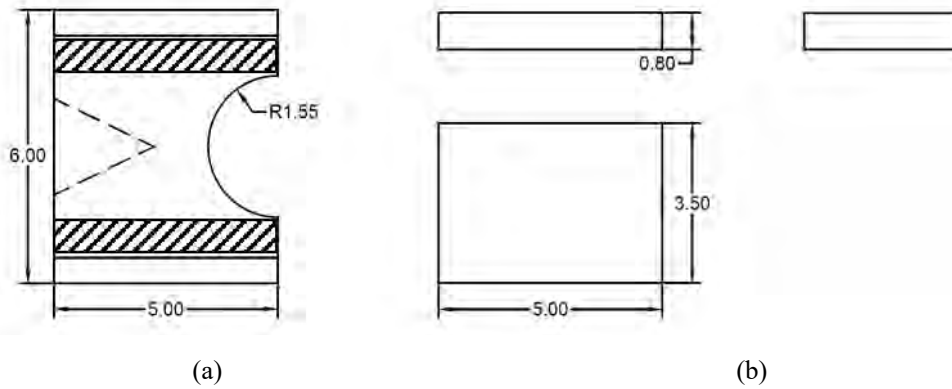
Figure 1 Schematic showing (a) tensile bar head dimensions and location of the cut (the marked area), and b) bend test sample dimensions (unit: mm).

Table 2. High dose four-point bend specimens tested in this report

Alloy/heat	Parent tensile sample ID	Four-point bend sample ID	Dose (dpa)	Thickness (μm)
316-1 E	B101	B101-B1	46.9	720-800
316-1 E	B89	B89-B1	67.4	800 ± 5
316-1 E	B35	B35-B1	125.4	830 ± 5
304-1 H	A84	A84-1-1	5.4	800 ± 5
304-1 H	A98	A98-1-2	69	935 ± 5
304-1 H	A96	A96-1-2	95	886 ± 5
304-1 H	A32	A32-1-1	125.4	913 ± 5

2.2   Microstructure Characterization

2.2.1   Micro-Hardness Measurement

Micro-hardness measurements were made to evaluate the bulk changes in the irradiated microstructure. Therefore, the electronically polished four-point bend samples were used to measure the Vickers micro-hardness at the University of Michigan. The indentation position is far away from the uniform strained region to avoid its effect on crack initiation. Each specimen was measured at a load of 200 gf, with at least 10 independent indents used to determine, whereas the average hardness and standard deviation were then recorded.

2.2.2   TEM Analysis

TEM samples were prepared from the as-irradiated CERT samples at LAMDA using an FEI Versa Dual Beam FIB-SEM. The FIB lift-outs were first thinned to around ~300 nm by 30 keV beam energy, and then were thinned and polished to a final thickness around ~100 nm by 5 keV and 2 keV to reduce FIB damages induced at high beam energy. The final thickness of the TEM foils for B89 and B35 was 150 nm and 120 nm, respectively. The thickness was measured using electron energy loss spectroscopy (EELS) in a JEOL 2100F TEM/STEM at the Michigan Center for Materials Characterization (MC^2) at the University of Michigan (UM). The uncertainty in thickness measurements is typically 20% [3]. The microstructures of the thin foils were characterized using a Thermo Fisher Tecnai G2 F30 TWIN TEM and a Thermo Fisher Talos F200X G2 S/TEM. Dislocation loops were imaged at different locations using g=1/2{311}. Frank loops were imaged using a dark-field, rel-rod technique [4]. The number of loops characterized is dependent on the number density and in the as-irradiated condition, 380 loops were characterized. Precipitate size and density were measured using conventional dark-field technique and TEM-EDX. Diffraction pattern technique and High Resolution (HR) Transmission Electron Microscopy (TEM) were used to identify the types of precipitates.

Radiation induced segregation (RIS) was assessed in the irradiated CW 316 SS. Energy-dispersive X-ray Spectroscopy (EDS) maps were taken from random high angle boundary using the FEI Talos microscope at the LAMDA laboratory at ORNL using a map size of 1024x1024 pixels with a resolution of ~0.23 nm/pixels with a probe full-width half max of ~1.5 nm. Each scan had a duration of one hour with more than 100,000 counts/sec with dead times from 1-6%. The Talos microscope has a much higher counting rate compared to typical STEM/EDS by virtue of the use of multiple EDS detectors. Before EDS measurement, the grain boundary was tilted to an edge-on position to maximize the spatial resolution of the measurement. Due to the limitation of available grain boundaries for RIS, only one grain boundary was measured, but multiple EDS maps were obtained from different segments of that grain boundary. The x-rays counts were converted to weight percentages using the Bruker Esprit© 1.9 software package, which uses the Cliff-Lorimer calculations for each pixel.

2.3   Test Systems and Procedures

2.3.1   Test Systems

The four-point bend testing systems IM2 is located in an irradiated material testing lab (IMTL) at UM. The water loop schematic diagram is shown in Figure 2. The water loop consists of two sub loops, loop 1 for conditioning the water at room temperature and low pressure, and loop 2 for simulating light water reactor environment at high temperature and high pressure. The environmental parameters such as conductivity and dissolved gas concentration are controlled in loop 1. The water is then pressurized and heated in loop 2, reaching the desired temperature and pressure in the autoclave and recirculated to the primary water column. The conductivity and dissolved oxygen (DO) are monitored at both inlet and outlet of loop 2.
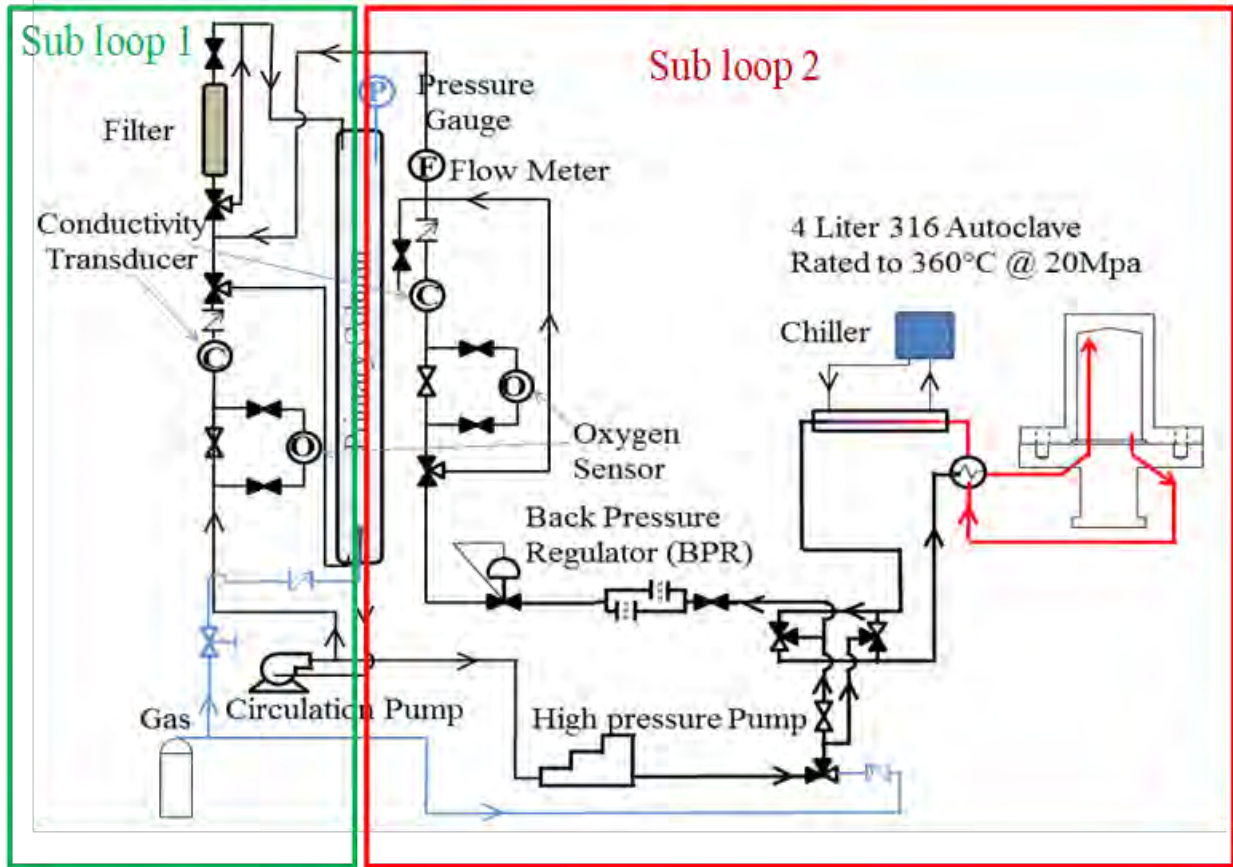
Figure 2. Schematic of the water loop used in the IM systems in the Irradiated Materials Testing Laboratory.

The IM2 loading system has one pull rod located in the center of the autoclave head, which was used to meet the requirement of fine control of the deflection of the four-point bend specimen (Figure 3). The application of load is using a 50 kN servo motor. A linear variable differential transformer (LVDT) is mounted on the pull rod to measure displacement. A load cell was connected with the pull rod, which was used to accurately measure the load applied to the sample. The pull rod is sealed at the feed-through into the autoclave with a self-energizing graphite seal with an internal spring that expands under pressure. The pull rod inside of the autoclave is connected to an Inconel 718 sample loading fixture. Electrical insulation is provided by zirconia washers located in the loading fixtures. After loading the specimens, the autoclave body is sealed to the autoclave head, thus preventing any leakage during the experiment.
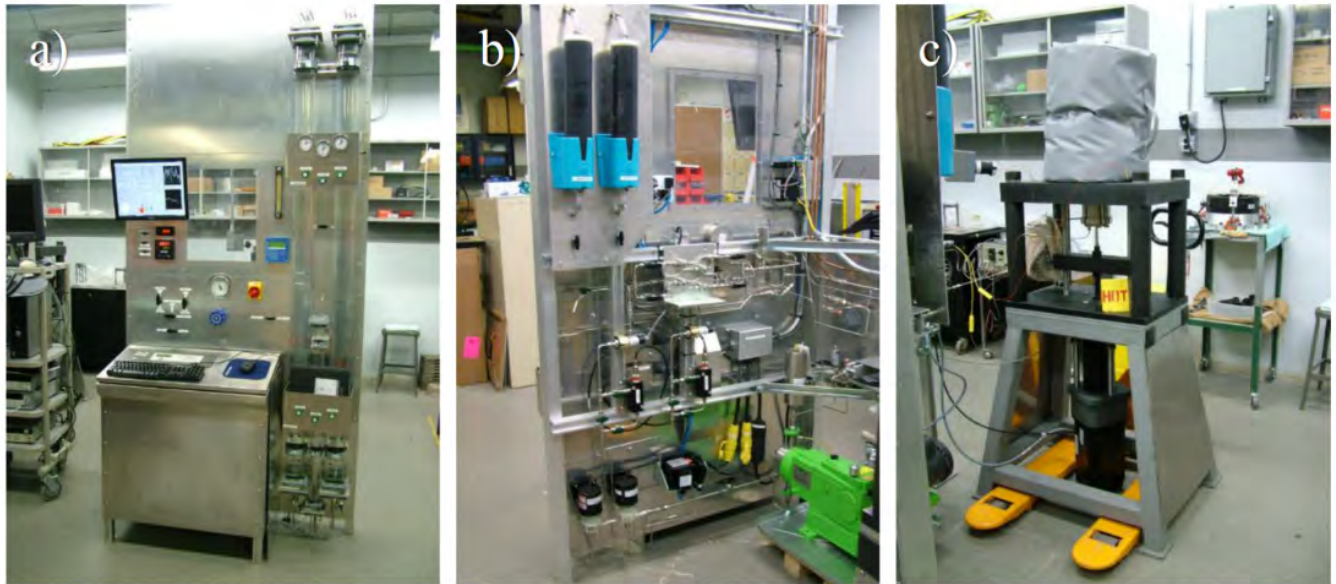
Figure 3. Images of the IM autoclave test system and water loop. a) Control panel front, b) control panel back with plumbing and sensors, and c) load frame, motor, and autoclave.

2.3.2   Procedures for Four-point Bend Test

Testing environment and strain rate.

Four-point bend tests were conducted in a simulated PWR environment. The environmental parameters and the statin rate are summarized in Table 3. The strain rate was lower to 4.3×10^{-8}/s which is 7 times lower the that used in CERT test (reported in the last year annual report) by virtue of the longer exposure time in high-temperature water.

Table 3. Environmental parameters and strain rate for four-point bend tests.

Parameter	PWR primary water
Temperature (°C)	320
Pressure (MPa)	13.7 (2000 psi)
Inlet conductivity (µS/cm)	21.53
H_2 concentration (cc/kg)	35
O_2 concentration (ppb)	<5
Boron as H_3BO_3 (ppm)	1000
lithium LiOH (ppm)	2
pH at 25°C	6.5
Strain rate	4.3×10^{-8}/s

Fixture for the four-point bend sample

The four-point bend test method was developed by Stephenson as reported in reference [5] and the detailed description of this method can be found in reference [6]. The four-point bend sample has a constant strain area of 0.5 mm × 3.5 mm, which makes it possible for us to locate the crack initiation site in a reasonable time. The four-point bend test fixture used for the study was fabricated from Inconel 718 alloy in accordance with the schematic shown in Figure 4. Heat treatment of post-fabricated fixture parts created a hardened state to prevent deformation during bend testing. Four round posts called centering pins, elevated from the bottom support surface by 0.4 mm, surrounded the sample to prevent rotational misalignment. Set screws to the left and right of the sample and centered the sample laterally and were retracted after pre-loading the sample to prevent constraint during bending.
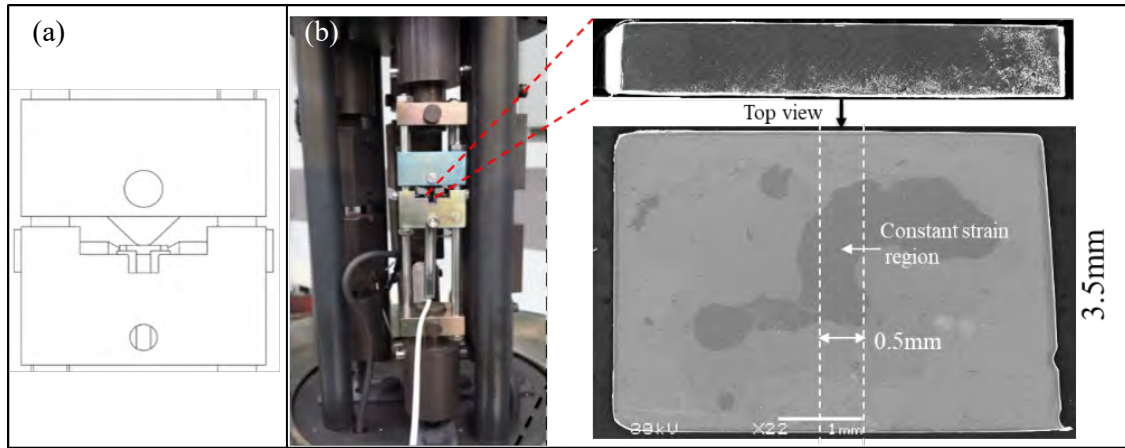
Figure 4. Schematic of the four-point bend loading fixture (a) and a photo of the fixutre including bend sample with side and top view (b).

System compliance at 320ºC in PWR

For the high-temperature tests, direct sample deflection measurements were not possible in high-temperature environments due to limitations of the electronics in the device, therefore estimations of sample deflection were made by subtracting a load-dependent compliance correction factor from the crosshead deflection measurement. This compliance correction factor was determined in 320°C primary water by loading a ~10 mm thick 'bend' sample (hardened Inconel 718) with the same cross-sectional geometry as the actual bend test samples for multiple times. From our prior experience, it was observed that the applied loads for neutron-irradiated materials were significantly lower than 220 lbs. Therefore, the compliance measurements included the entire range of loads applicable to neutron-irradiated materials. Subtraction of the compliance from the measured crosshead LVDT displacement gives an approximation to the actual deflection at the sample surface. Due to its large thickness, it was assumed that no sample deflection occurred during loading, and compliance correction curves were determined by fitting a cubic polynomial to the resulting load vs. crosshead displacement curves, as shown in Figure 5. Compliance correction curve determination was repeated twice for accuracy and averaged to determine the following correction factors in 320°C primary water:

$$CF_{PW} = 2.03931 \times 10^{-5}P^3 - 0.01072 \times 10^{-5}P^2 + 3.39312P - 165.28 \tag{1}$$

where P is the applied load in N and CF_{PW} is the correction factor in the PWR environment in μm.
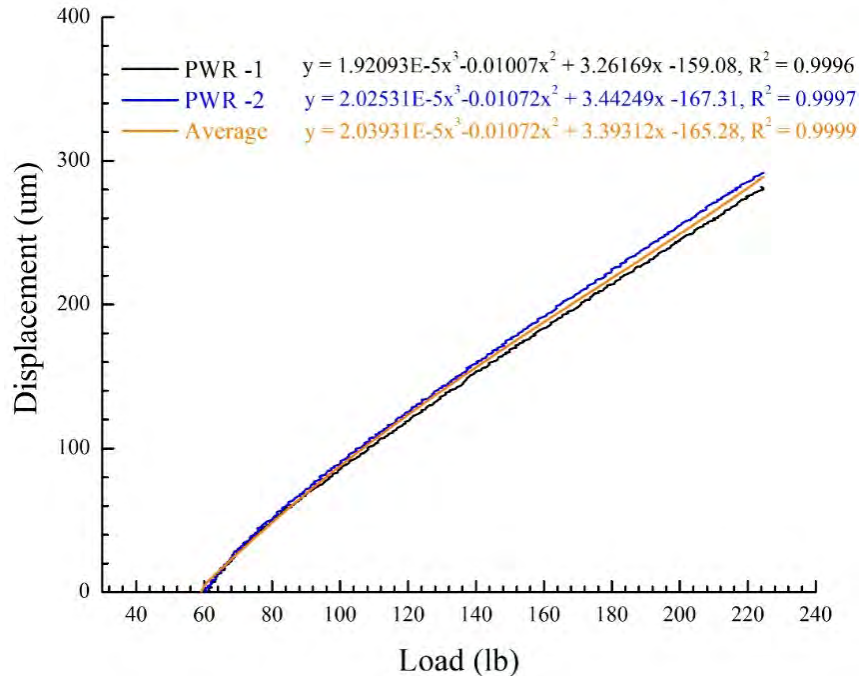
Figure 5. Compliance measurements for the four-point bend test in single specimen configuration in PWR primary water. The averged curve was used to calulate the displacment of the bend smaple. -.

Interrupted strain test for four-point bend sample

Four-point bend tests were carried out using the IM2 system in IMTL at UM. Bend samples were loaded on the fixture with a tailor-made tweezer, centered by tightening the set screws on either side uniformly and held in place by bringing the loading points into contact with the sample and lightly tightening the connection of the pull rod at the system crosshead. Sample bending was performed by moving the crosshead at a constant rate of 1.67×10^{-8} in/s, generating a strain rate of 4.3×10^{-8} s^{-1} on the polished surface, until achieving the desired amount of load. The target stress in the constant strain region was achieved by applying a corresponding load based on the linear behavior of stress with load, as shown in Figure 6. The relationship between the bend yield load in four-point bend and the tensile yield stress was formed utilizing previous experimental data on neutron-irradiated 304 stainless steel specimens by Kale Stephenson et al. [5] and benchmarking experiments utilizing a heat of 316 SS cold-worked to varying degrees. While there is some variability, this comparison allowed a prediction of the bend yield load based on previous measurements of the tensile yield stress. Due to the linear relationship, it was assumed that loading to a percentage of the bending yield load in a four-point experiment is directly comparable to loading to that percentage of the yield stress for the specimen.

There is a tare load applied to the bend specimen by the vessel water pressure that is not directly measured by the pull rod load cell. With a 4.76 mm diameter pull rod and the 2000 psi system pressure, a tare load of 55.4 lb (246.5 N) was added to the bend specimen, under simulated PWR conditions. The testing was performed in increments to create crack initiation and limit the amount of crack propagation in the material. Increments are reported in this report as the fraction of irradiated yield stress.
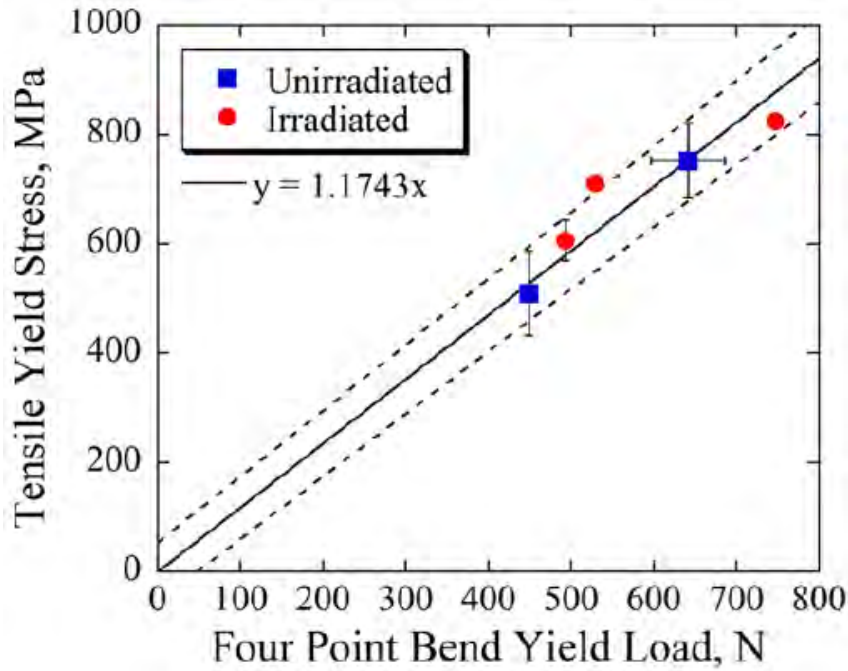
Figure 6. Comparison between the measured tensile yield stress and four-point bend yield load for several specimens, both irradiated and unirradiated. The linear fit was utilized to predict the bend yield load for conditions previously strained in tensile experiments.

The relationship between bend yield load and tensile yield stress was obtained from specimens with a thickness of ~800 μm. In a four-point bend experiment the maximum bend stress, σ_{max}, is directly related to the specimen thickness. The maximum stress in the tensile surface is inversely proportional to the square of the thickness [7], as described by the following equation.

$$\sigma_{max} \propto \frac{1}{h^2} \qquad (2)$$

Therefore, the applied load was adjusted based on the thickness of the sample when a certain fraction of yield stress was targeted.

Crack Initiation Detection

The bending experiments were conducted in small increments such that we could more precisely identify points of crack initiation and study the microstructure responsible for crack initiation. After each stress increment, the specimen was removed from the autoclave and was examined using a JEOL JSM-6480 SEM. The uniform-strain region was imaged under 1000X magnification in BSE mode to record any sites of crack initiation as well as changes in the localized deformation. The GBs that are darker and wider than the others in BSE mode is most likely to change into cracks in the next strain test. Therefore, dozens of GBs with that kind of features were traced after each stress increment to record the change in GBs and its surroundings. Hence, the evolution of cracks and the microstructures that are responsible for crack initiation can be determined. Higher magnification images were taken when the crack initiation was observed. The cracks and microstructure features at the crack initiation sites were characterized and their relationship with cracking was analyzed. By analyzing the microstructure at the crack initiation sites, one can understand how this affects the crack initiation.

9

Determination of the strain condition

In theory, there will be no plastic deformation in the constant strain region during elastic straining. However, slippage of the sample on this stage, the imperfect setting of the sample on the stage, or non-uniform thickness of the sample might result in plastic deformation even though the applied load was much smaller than the yield load. To confirm that no plastic strain occurred during the bending test in the elastic stain region, the deflection of the sample was measured multiple times in the constant strain region after each stress increment. The amount of deflection was measured *ex-situ* by comparing the change in deflection for each of the leading edges through compiled SEM images as seen in Figure 7. If the measured deflection of leading edges is less than 2 μm or within the error bar it means that the sample was not plastically deformed. If the sample was believed to be plastically strained, the strain amount in the tensile surface can be calculated using the relationship given in Figure 8.

Figure 7. Compiled images of the entire Edge 1 for non-irradiated 304 in air: a) edge pre-straining, b) edge post-straining. A clear amount of plastic deformation occurred in the center of the specimen during the plastic straining increment. The plastic deflection is measured as the change in central 500 μm between the pre- and post-strain images.
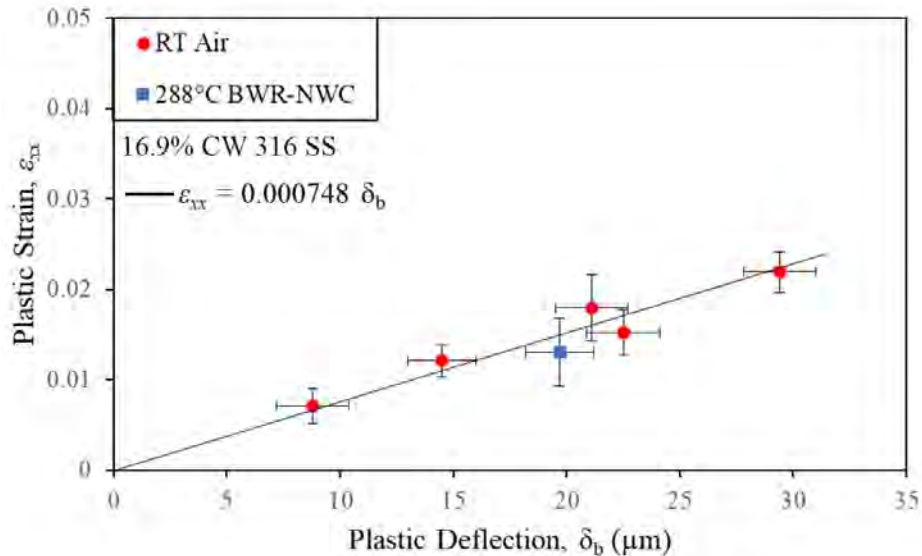
Figure 8. Comparison of the measured plastic strain, via a grid of fiducial indents, and the plastic deflection, via side profile measurements, for unirradiated stainless steel. The identified linear relationship was used to predict bend strain at low deflection values.

2.4   Establishment of cracking standard

2.4.1   Definition of cracking

Crack initiation is a concept that is difficult to define and varies in different conditions. The scientific definition is that it is the formation of a mechanically distinct geometry that will tend to grow in preference

to its surroundings. However, practically, it is the detectability that is likely to be achieved in-situ for a laboratory autoclave experiment. Also as reported in reference [8], the width of an IG crack tip is less than 5 nm, indicating that crack width could be very small when cracking occurs. Therefore, to detect the crack with our available SEM equipment and determine the correlation of microstructures with crack initiation, a standard for the cracking of GB must be established.

Figure 9a shows a crack from the tensile sample B89. It is well accepted that this is a crack as we can see the grain facet clearly down the crack. One common feature shared by all the cracks is that the crack is bounded by two bright lines which are believed to be the edges of the crack, and are created by the effect of the sharp curvature of the edges on the secondary electron (SE) production. The plot of gray value across the crack is given in Figure 9b, which was processed using ImageJ® software. The two peaks correspond to the two bright edges. Therefore, it implies that the GB has been apart when two bright edges along the GB were observed in the SE image. Henceforth, this standard will be used to determine whether the GB is cracked or not.
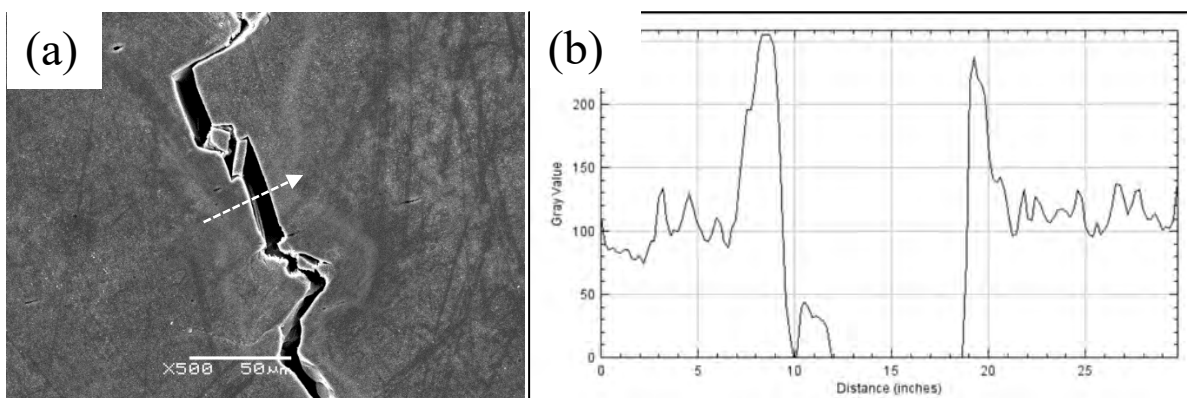
Figure 9. A well-defined crack from the tensile sample B89 (a) and the gray value plot taken at the dashed line (b).

2.4.2 State of GBs after exposure to high-temperature water

Four GB states were observed after exposure to high-temperature water: intact, oxidized, suspected crack, and cracked, and are differentiated by the shape of the gray plot. As shown in Figures 10a&b, the intact GB is barely visible in the SE image and the gray value over it is irregular and noisy. However, the GB is more clear after oxidization, and gray value is less noisy, showing a "V" shape, Figures 10c&d. Figures 10e&f show a suspected crack and the gray value along the dashed line. There is only one bright line along with the GB and accordingly only one peak in the gray value plot. Though it looks like a crack it does not meet the cracking criterion we established. Hence, the GB meets this condition will be treated as a suspected crack. Figures 10g&h show a crack and the gray value along the dashed line. Two bright lines can be seen in the SE image as well as two peaks in the gray value plot. The distance of peak-to-peak is defined as the width of the crack. For example, the width of the crack shown in figure 10g is ~100 nm. For now, the cracking standard has been established and will be used in this study. The image used to determine the state of the GB was taken at 15000x. This is the maximum magnification that our SEM equipment can go without compromising too much of the resolution.
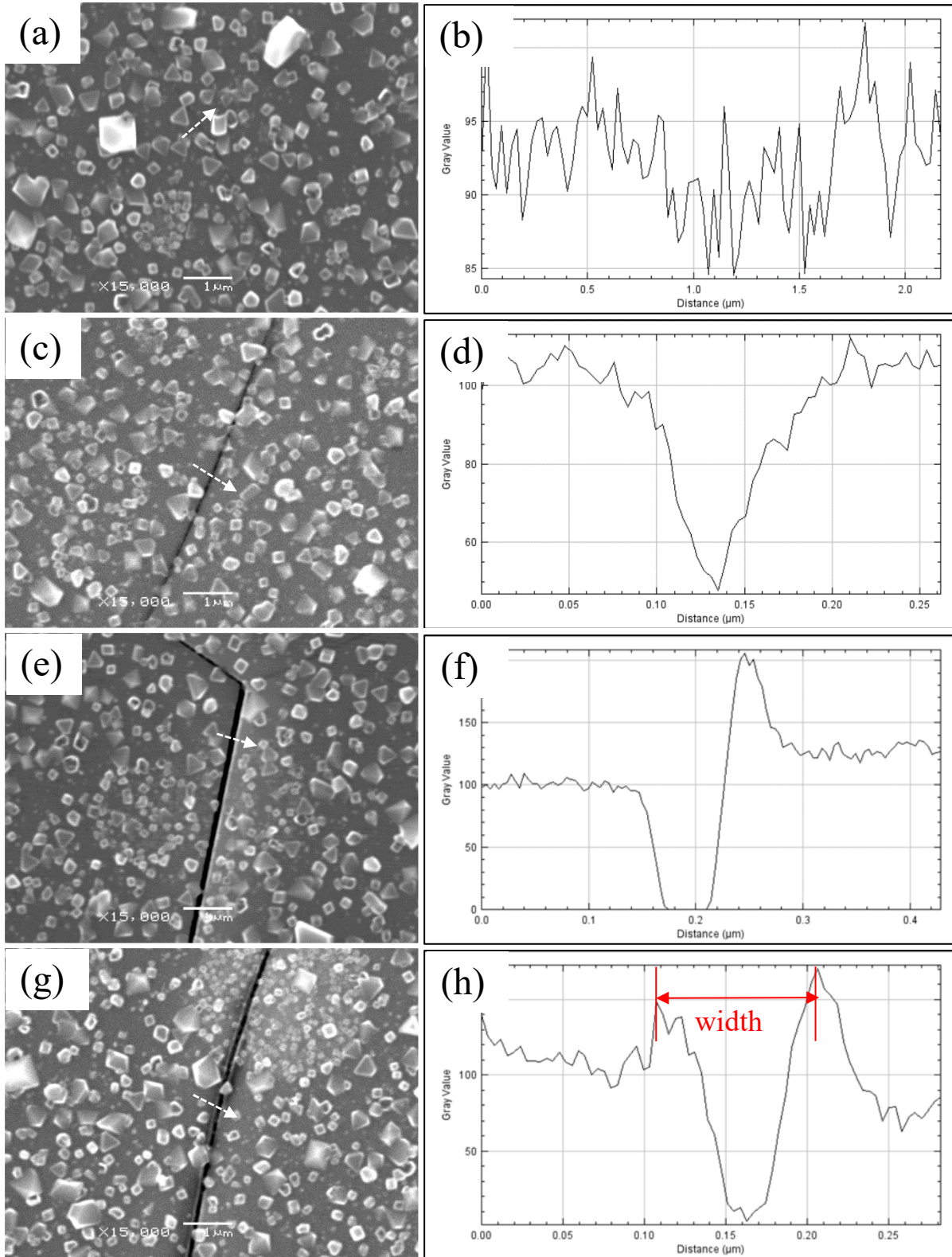
Figure 10. Intact GB after exposure to high-temperature water (a) and the gray value (b), an oxidized GB (c) and the gray value (d), a suspect crack (e) and the gray value (f), a small crack (g) and the gray value (h).

3. RESULTS

This section presents a summary of the results of microstructural analysis completed on the 316 SS samples. The microstructural analysis includes the Vickers micro-hardness, dislocation loop size and density, precipitate size and density, and grain boundary segregation. Majority of the content in this part is from four-point bend tests on CW 316 SS and SA 304 SS samples. Straining behavior of the sample will be presented first and then the crack initiation and propagation phenomenon was described. Finally, the characterization results of crack were analyzed.

3.1 Hardness

Vickers micro-hardness has been often reported in the literature as a simple method to evaluate the bulk changes in the irradiated microstructure. The micro-hardness of three CW 316 SS samples and four SA 304 SS samples of different dpa were measured using the indenter located at Phoenix building 1066 at the UM. The hardness measurements for the samples are shown in Table 4. The YS of materials obtained in the CERT test was also summarized in this table. The hardness of CW 316 SS samples shows a little bit change with the variation within the measurement error and the yield strength shows a similar trend. For the SA 304, the YS of 5.4 dpa sample is smaller than higher dpa samples, however, the difference is not significant. The hardness is believed to be saturated between 5.4 and 69 dpa.

Table 4. Micro-hardness in the CW 316 and SA 304 samples

Alloy	CW 316			SA 304			
dpa	46.9	67.4	125.4	5.4	69	95	125.4
Hardness (Hv)	424.3±10.3	413.2±8.6	415.1±9.4	357±8.2	392±9.3	400±8	397±9.8
Yield strength (MPa)	1020	1017	1024	794	834	832	826

3.2 Irradiated Microstructure

3.2.1 Deformation twins

As the samples were ~15% cold-worked, they contained a large number of twins, as shown in Figure 11, that survived after irradiation. However, line dislocation networks disappeared, similar to that reported by Renault et al. [9]. This phenomenon was also reported by Edwards et al. [10], Fukuya et al. [11], and Miao et al. [12] in neutron-irradiated 316 SS (flux thimble tubes).
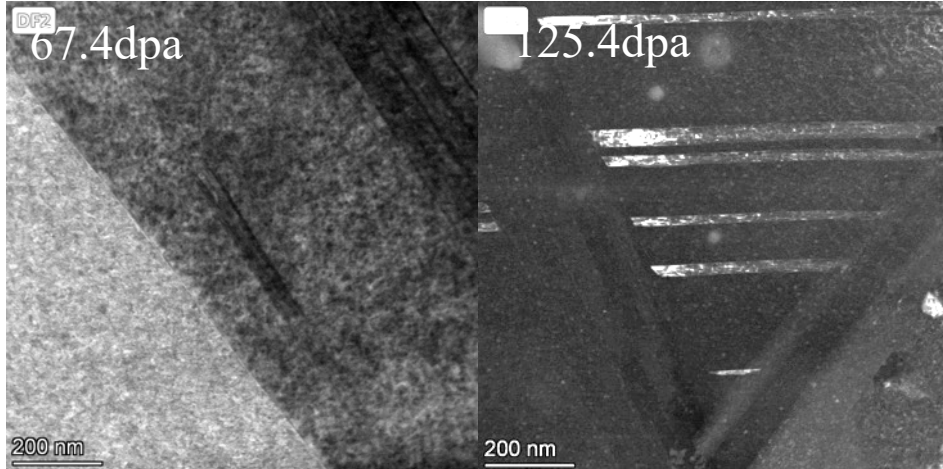
Figure 11. Deformation twins are survived after irradiation in high dpa samples.

3.2.2 Dislocation Loops

The faulted dislocation loops in the 67.4 and 125.4 dpa samples were characterized using a rel-rod dark field technique. TEM images of dislocation loops are shown in Figure12. Both of the dark field images show a large number of dislocation loops and the population shows no big difference. The number was counted and the size was measured using Photoshop®. The average diameter and number density are given in Table 5. The average loop size is 9.6 nm and 8.9 nm for 67.4 dpa and 125.4 dpa samples, respectively. The density is also similar and falls into the range of 5-6 x 10^{23}/m³. The size distribution of dislocation loops is shown in Figure 13. Two samples show almost the same shape over the size of loop diameter and most of the loops are smaller than 15 nm with a dominant number close to 7 nm.
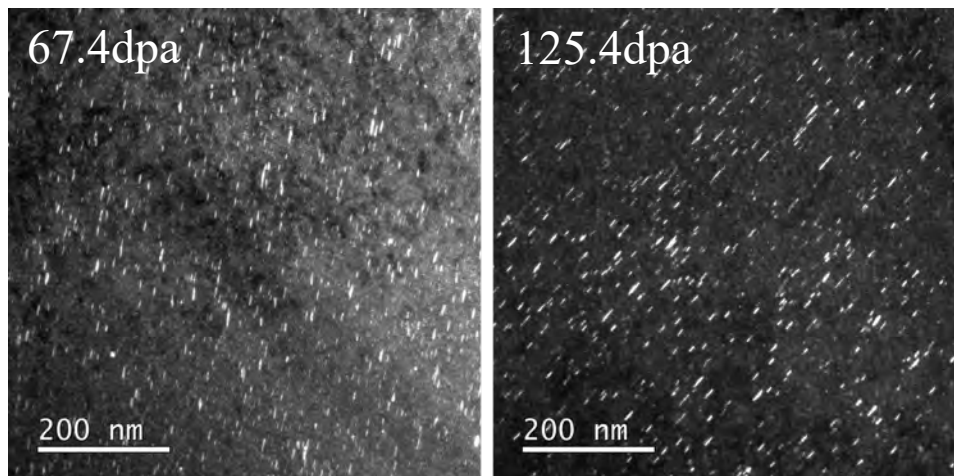
Figure 12 Rel-rod dark-field TEM images (g=1/2{311}) showing the faulted dislocation loops in CW 316 SS.

Table 5. Dislocation loop size, number density in two different dpa samples.

Alloy	Dose (dpa)	Loop density (x10^{23} m^{-3})	Loop diameter (nm)
CW 316	67.4	0.5	9.6±1.5
CW 316	125.4	0.6	8.9±1.8
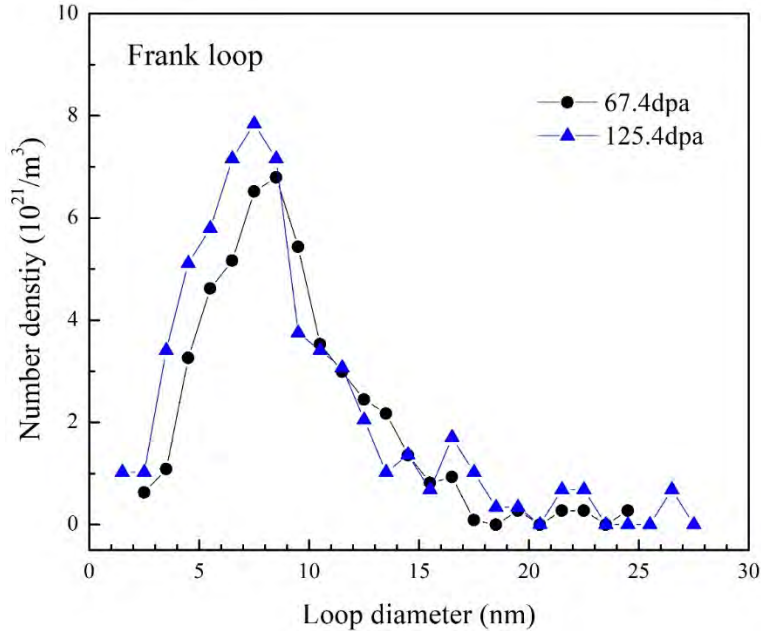
Figure 13. Comparison of the size distribution of dislocation loops in CW 316 SS samples.

3.2.3   Precipitates

Ni-Si rich precipitates in the 67.4 and 125.4 dpa samples were characterized using a centered dark field technique. TEM images of precipitates are shown in Figure14. The number was counted and the size was measured using Photoshop$^{®}$. The average size and number density are given in Table 6. The average precipitate size is 5.0 nm and 8.3 nm for 67.4 dpa and 125.4 dpa samples, respectively. The number density is in the range of 1.4-3.5 x 10^{21}/m^3. It appears that the number density of precipitate in 125.4 dpa sample is larger than 67.4 dpa sample. The size distribution of precipitate is shown in Figure 15. The size variation is smaller than dislocation loops and all the precipitates are smaller than 11 nm.
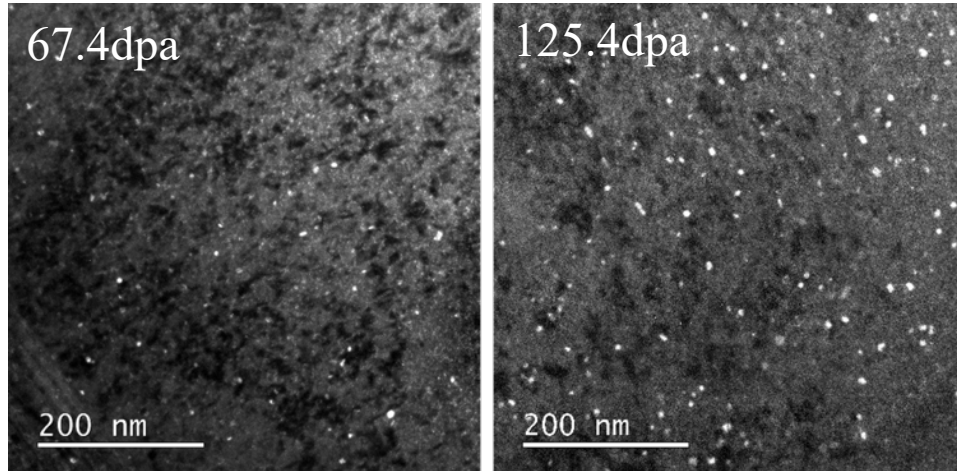
Figure 14. Dark-field TEM images showing precipitates in CW 316 SS.

Table 6. Precipitate size, number density in two different dpa samples.

Alloy	Dose (dpa)	Precipitate density ($\times 10^{21}$ m^{-3})	Precipitate size (nm)
CW 316	67.4	1.4	5.0±1.9
CW 316	125.4	3.5	8.3±1.2
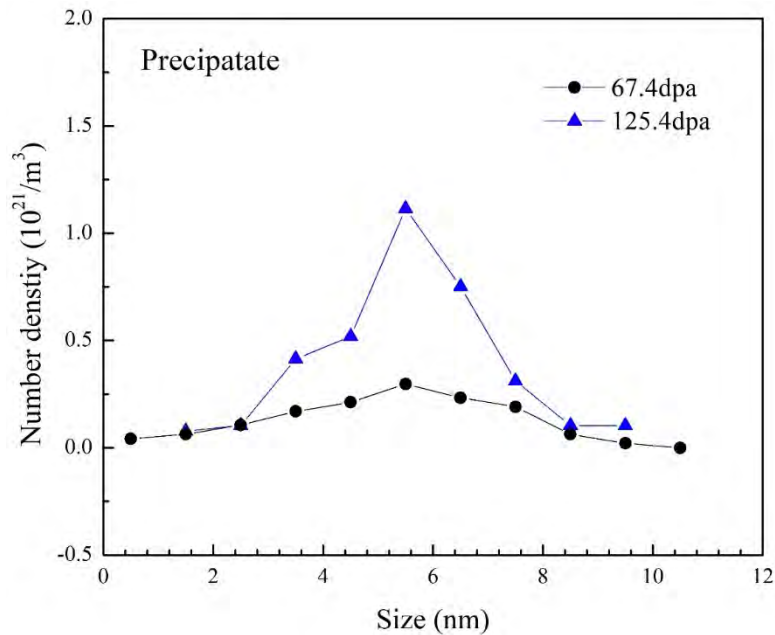
Figure 15. Comparison of the size distribution of precipitates in CW 316 SS samples.

3.2.4   Grain Boundary Segregation

Radiation-induced segregation was examined in CW 316 SS. Figure 16 and Figure 17 are the elemental images showing segregation of Cr, Fe, Mn, Ni, Si, and S at the high-angle and twin grain boundary in the

67.4 and 125.4 dpa sample, respectively. The deformation twin boundary is a defect sink and it can interact with the vacancy and interstitial fluxes result in the segregation of elements. The regions with enriched Ni and Si in the grain interior are associated with Ni-Si clusters or γ' precipitates due to the internal sinks produced during cold work and/or irradiation.
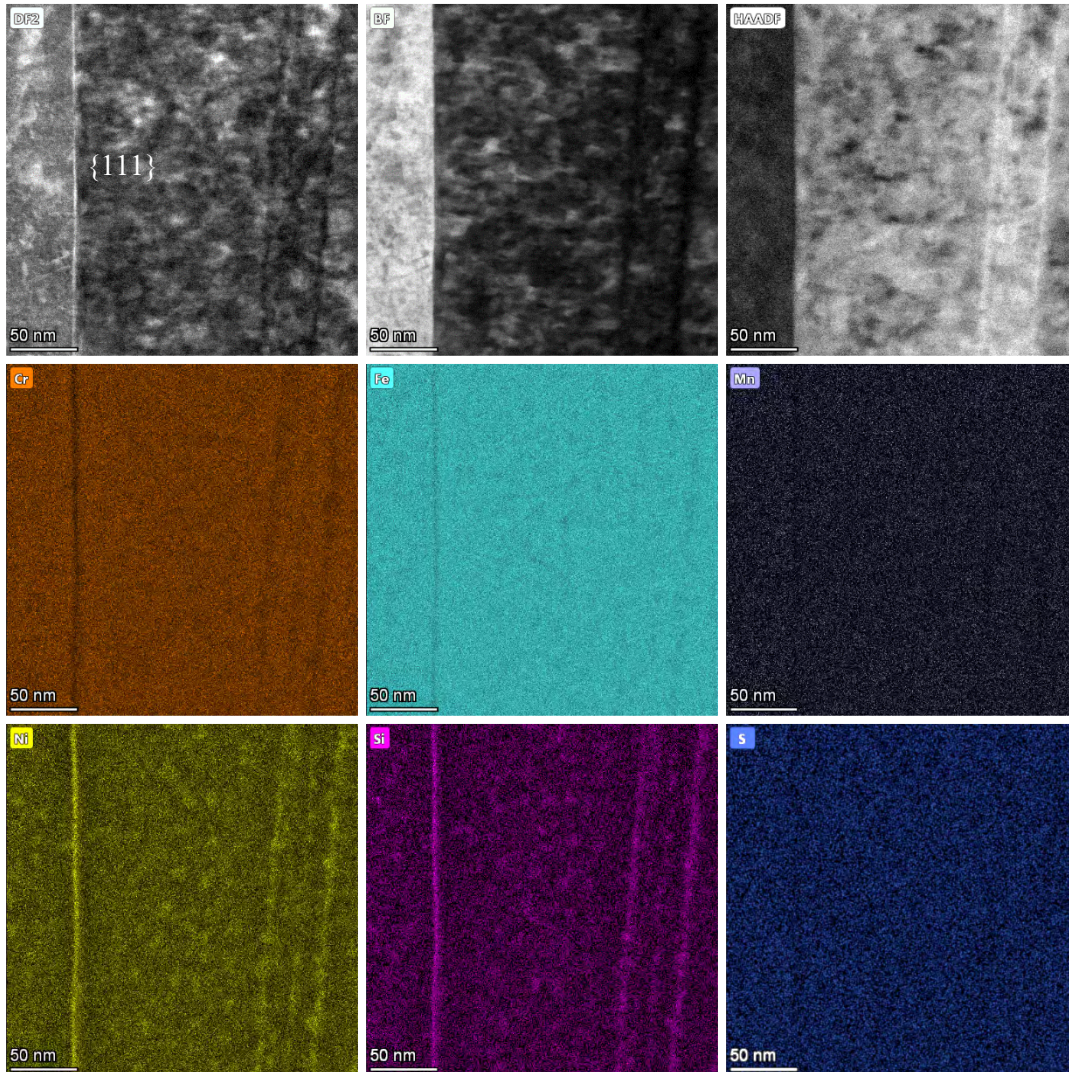
Figure 16. Radiation-induced segregation in CW 316 SS irradiated to 67.4 dpa as revealed by ChemiSTEM image. The depletion of Cr and Fe and enrichment of Ni and Si are evident.
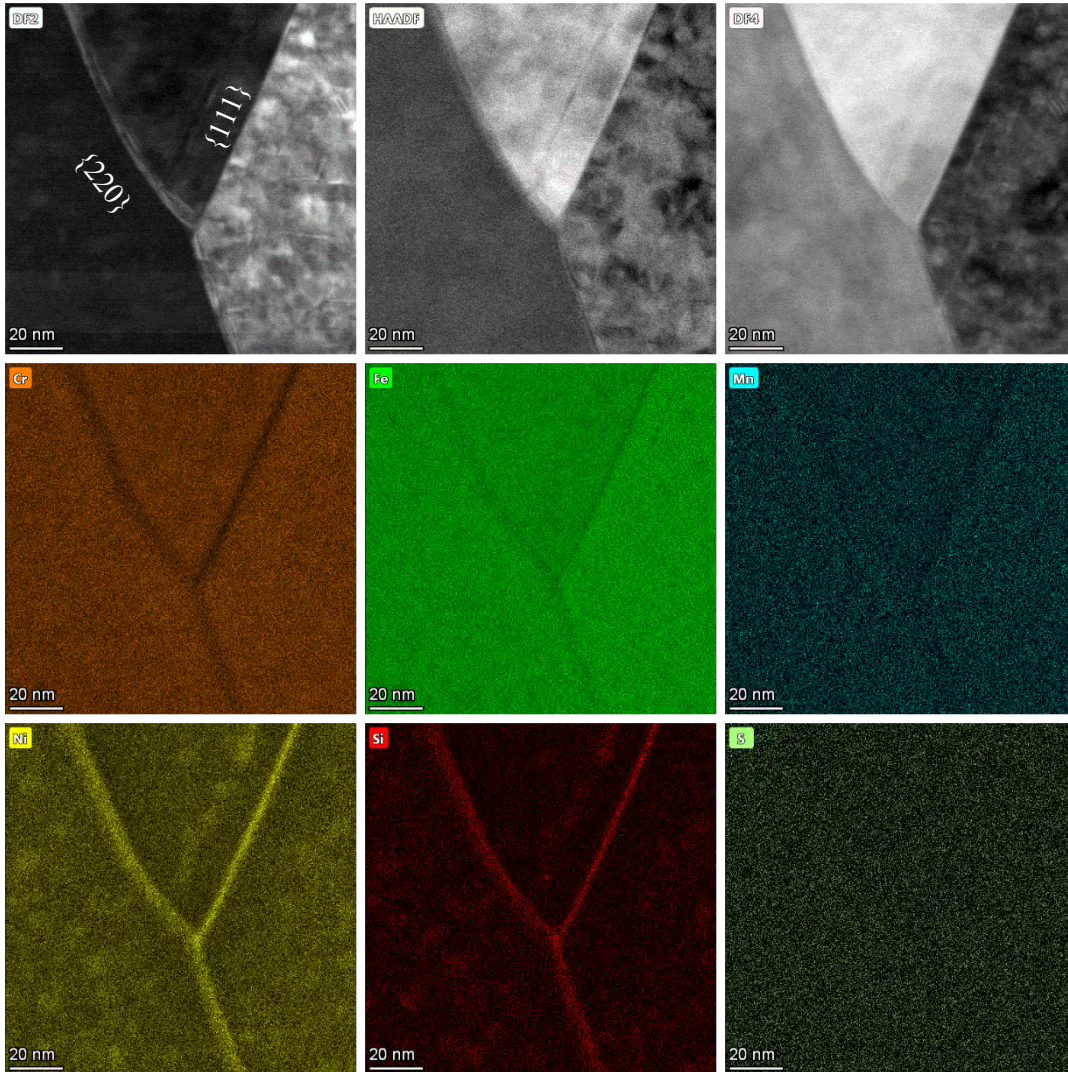
Figure 17. Radiation-induced segregation in CW 316 SS irradiated to 125.4 dpa as revealed by ChemiSTEM image. The depletion of Cr and Fe and enrichment of Ni and Si are evident.

3.3   Bending Test Results of CW 316 SS

This section presents the four-point bend test results from irradiated CW 316 SS samples tested by incremental loading. Load-LVDT displacement curves were provided, followed by the examination of surface and long edges of the bend sample in the uniform strained region after load increment. Cracks that initiated in the uniform strained region were fully characterized and quantified.

3.3.1   Interrupted Strain Behavior

The load was applied to a four-point bend sample by controlling the crosshead moving at a constant rate 1×10^{-6}/s. The crosshead immediately reversed its direction of travel and returned to the initial set point when the desired load was achieved. Ex-situ characterization in the SEM was conducted following each step. Figures 18-20 show plots of load vs. LVDT displacement. Tare load imposed on the bend sample was also added when those lines were plotted. From these figures, the load applied to achieve the target stress

in the tensile surface is known. The load and LVDT displacement showed a very good linear relationship when the load was increased, while the line curved when the load was reduced. The stress increment was determined as ΔYS= 0.2YS by referring to reference [13] because no cracks initiated in the as-irradiated 5.9 dpa sample in the elastic strain region. Hence, the sample B101-B1 was strained to 0.4YS and no cracks were observed in the uniform strain region. However, dozens of cracks initiated after staining the sample to 0.6YS. To study how the crack develops with load, the sample was further strained to 0.8YS.

Figure 19 shows the interrupted strain results of B89-B1. As dozens of cracks initiated in B101-B1 at 0.6YS, the initial stress on B89-B1 was set at 0.4YS and then 0.5YS. Similar to sample B101-B1, no crack initiated in this sample after straining to 0.4YS. However, as expected, few cracks (7) initiated in the sample after staining to 0.5YS. Characterization of each crack was conducted using the SEM. To study how the crack develops with load and compare the results with B101-B1, the sample was further strained to 0.6YS. More cracks were generated in the sample after straining to 0.6YS. The crack length, maximum width, and trace inclination to loading axis were measured.

Figure 20 shows the interrupted strain results of B35-B1. Catching initiation of the first crack in an irradiated sample is critical to reveal the factors that are responsible for crack initiation. Therefore, the initial stress increment was reduced to 0.4YS followed by a stress of 0.45YS. The same case happened to this sample that no crack initiated in this sample after straining to 0.4YS. Only one crack was observed in this sample after straining to 0.45YS. Images of the crack were taken and EDS analysis over the crack was also performed. To compare the results among the different samples, the stress was further increased to 0.5 and 0.6YS.
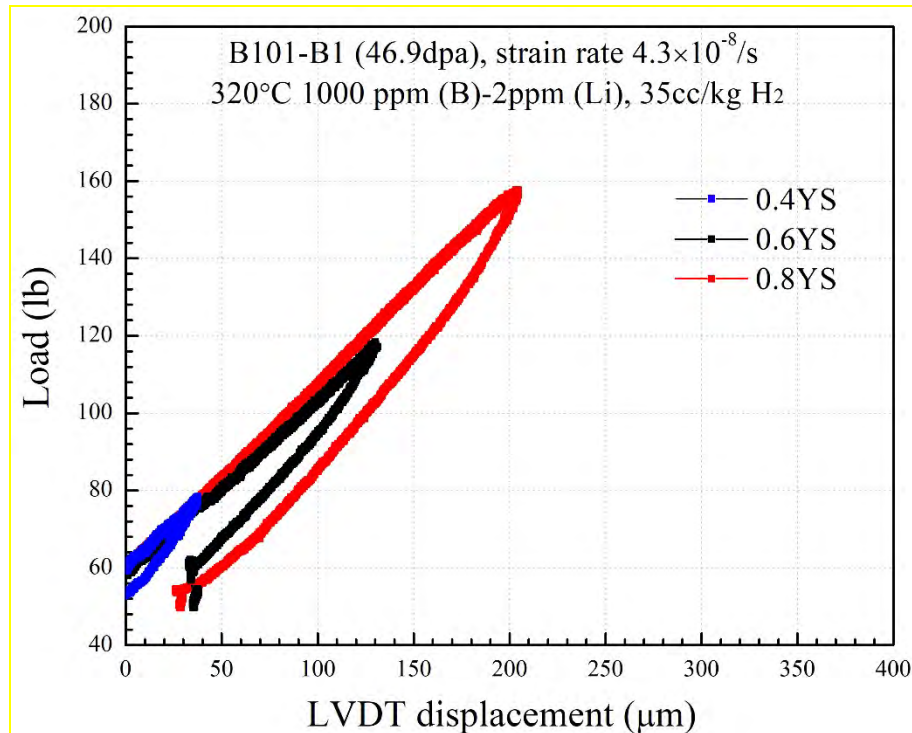
Figure 18. Load vs LVDT displacement for the sample B101-B1 (46.9 dpa) in primary water. Cracks in the sample were observed after straining to 60% of the irradiated yield strength.
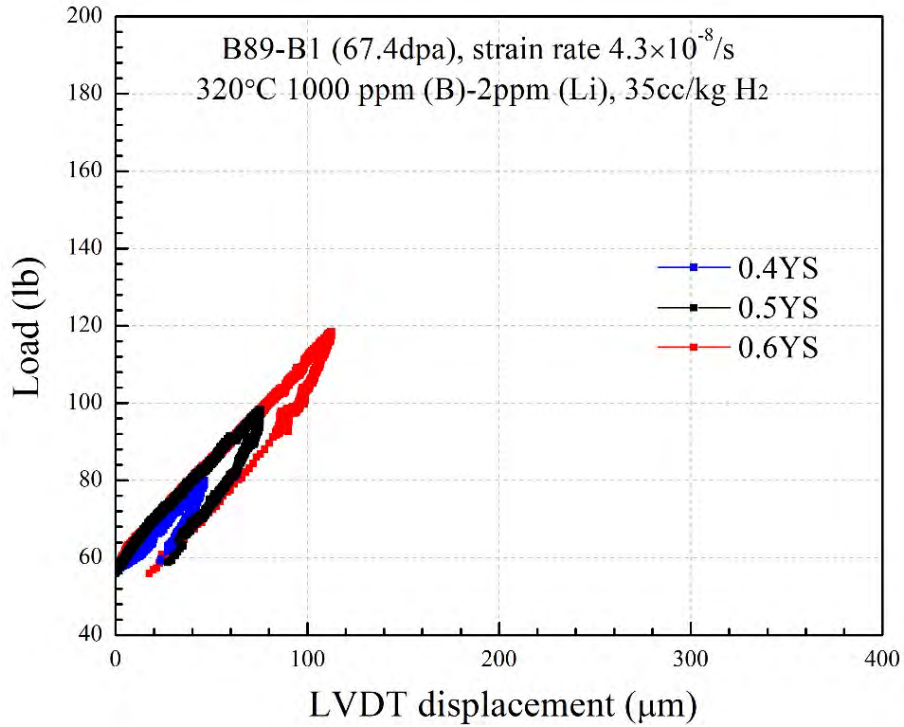
Figure 19 . Load vs LVDT displacement for the sample B89-B1 (67.4 dpa) in primary water. Cracks in the sample were observed after straining to 50% of the irradiated yield strength.
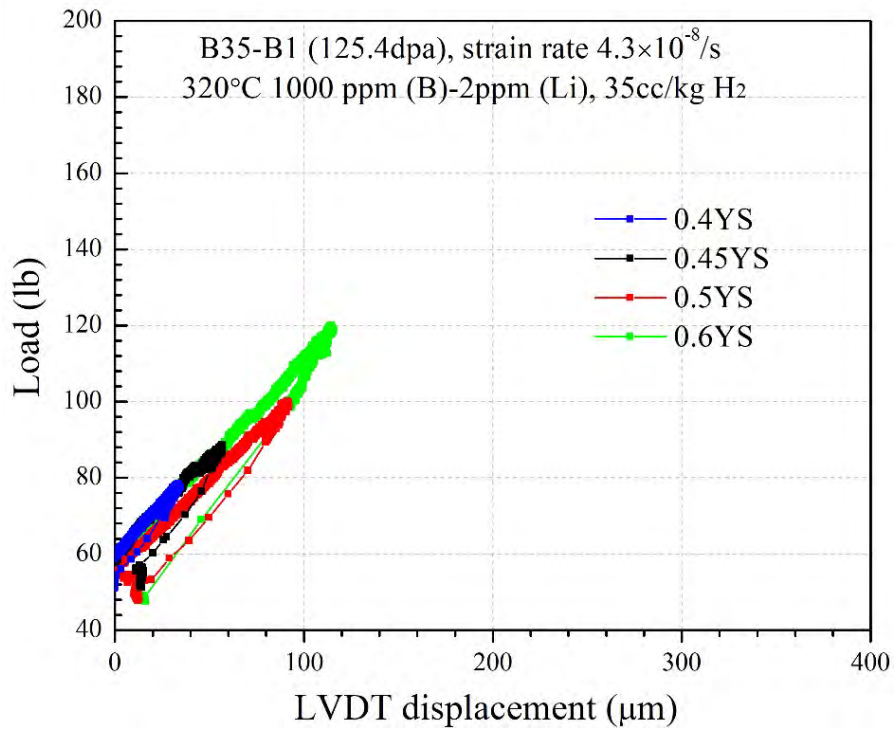
Figure 20. Load vs LVDT displacement for the sample B35-B1 (125.4 dpa) in primary water. Cracks in the sample were observed after straining to 45% of the irradiated yield strength.

Figure 21 shows the morphology of four-point bend samples after the last strain test. The yellow dashed lines outlined the uniform strained region in each sample. A large crack starts from the upper edge of the sample can be seen in the sample B101-B1, however, the cracks in the other two samples cannot be seen due to their small sizes and the low magnification of the images.
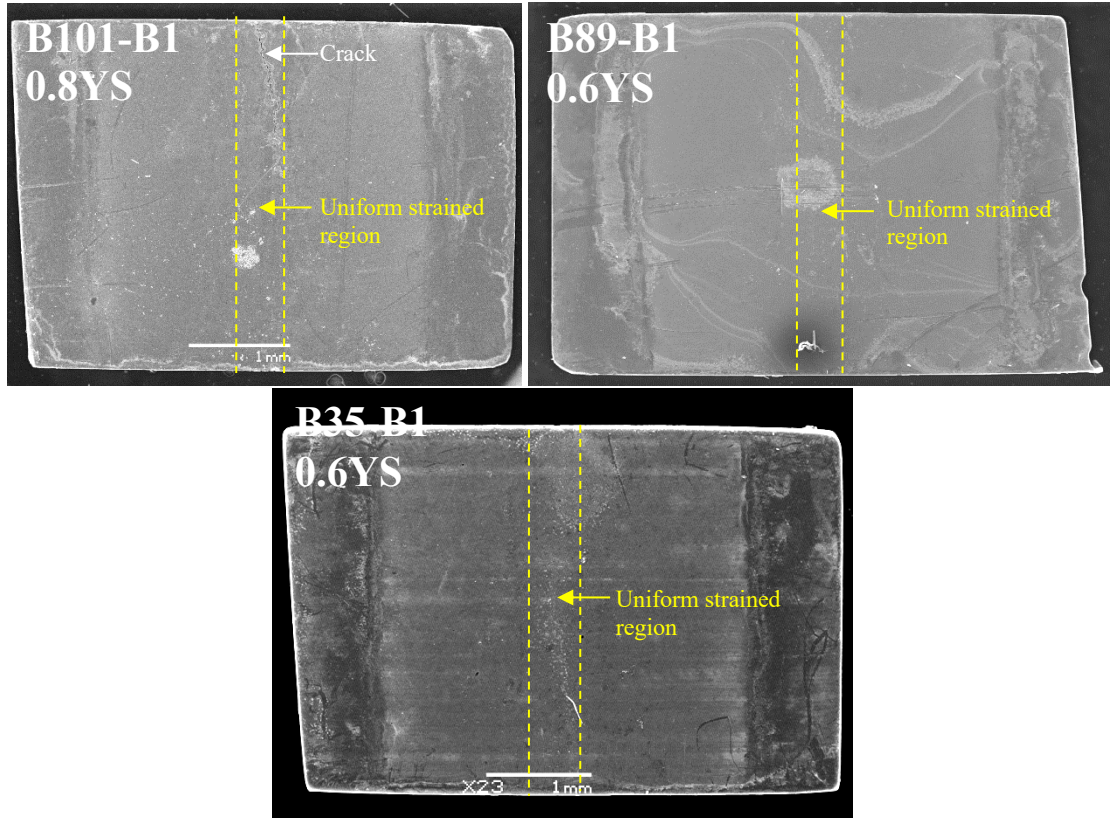
Figure 21. The morphology of four-point bend samples at the end of the tests.

3.3.2 Crack Initiation and Propagation

All the CW 316 SS bend samples cracked at a stress level well below their irradiated yield strengths, as summarized in Table 7. Crack initiated at as low as 45% of the irradiated yield strength in sample B35-B1. This result shows good agreement with reference [5] where the same test method and similar samples (irradiated in BOR-60) were used. Figure 22 shows representative cracks that appeared at a time when the crack initiation was observed for the first time. As a higher load was applied to B101-B1 the typical crack in this sample is much longer and wider.

Table 7. Crack initiation stress for the CW 316 SS samples.

Sample ID	Dose (dpa)	Initiation stress (% of YS)
B101-B1	46.9	60
B89-B1	67.4	50
B35-B1	125.4	45
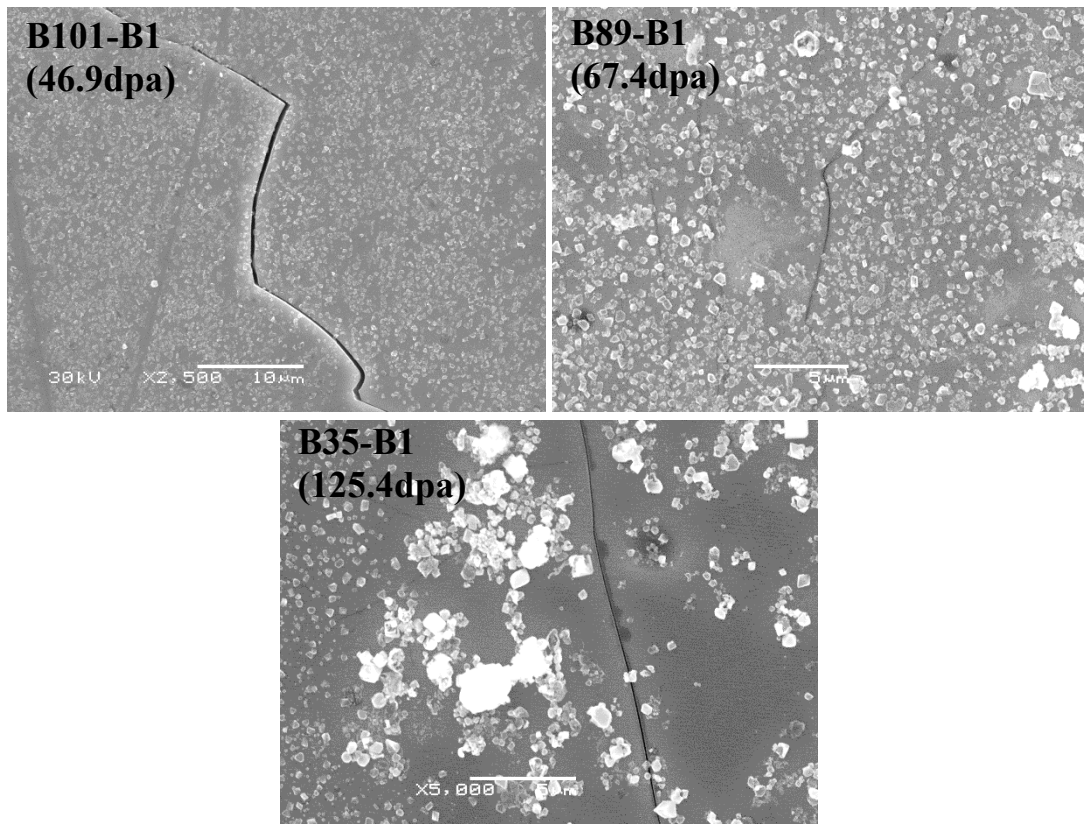
Figure 22. Representative cracks in CW 316 SS samples when the crack initiation was observed for the first time.

Figure 23 shows the first crack initiated in sample B35-B1 (125.4 dpa) and the EDS line scan results over the GB in the same position at different stresses. Figure 23a shows a typical surface morphology at 0.4YS. Figure 23b is a higher magnification image of the framed area in Figure 23a. The grain boundary is decorated with dark regions (indicated by yellow arrows) that are clearly shown due to oxidization. An EDS scan over the intact GB and dark regions shows enrichment of O and Cr (Figure 23e). Figure 23c taken after straining to 0.45YS shows no significant difference in morphology from the previous condition. However, a closer observation (Figure 23d) reveals that oxidized GB is fractured. An EDS line scan at the same location as previously shows a sharp drop of oxygen content (Figure 23e) at the position corresponding to the GB, which further confirms the separation at the boundary. Though no step-like features, as reported in the references [5, 13, 14] were observed in SEM images, the possibility of the formation of dislocation channels (DCs) cannot be excluded. The DCs may still be at the initial stage and are very faint, which makes them very difficult to be distinguished from numerous deformation twins under BSE.
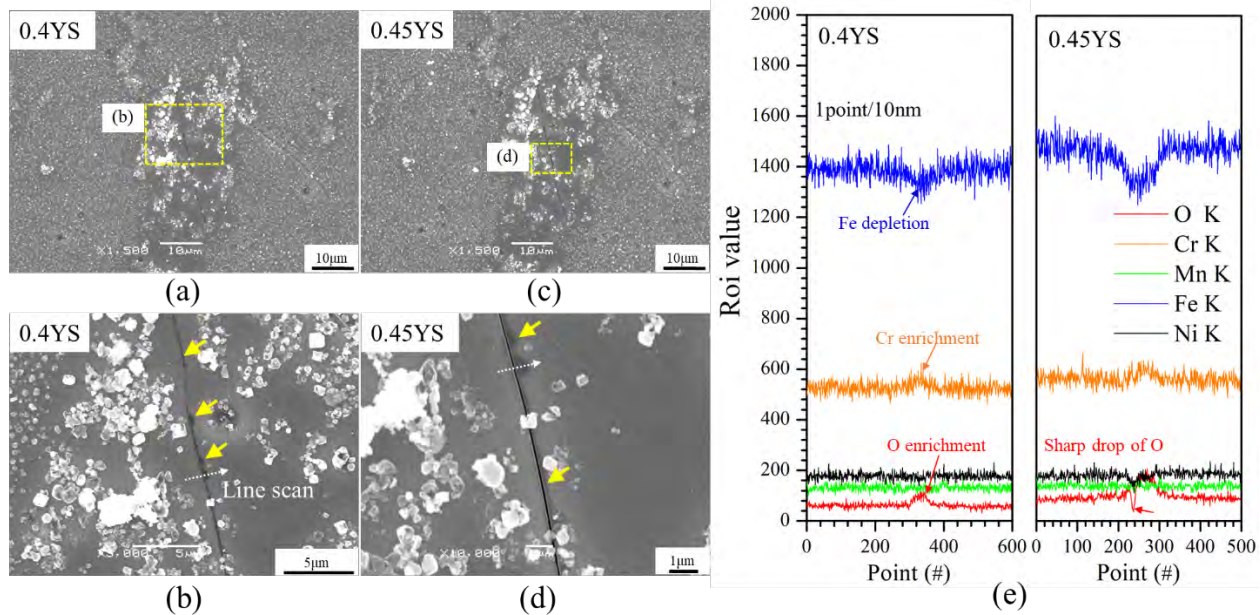
Figure 23. The first crack initiated in B35-B1 (125.4 dpa): (a-b) GB oxidization at 0.4YS, (c-d) crack initiated at 0.45YS, (e) EDS line scan results at the same position but different stresses.

Figures 24-26 present cracks developed in CW 316 SS samples. They provide a good opportunity to understand how cracks behave with the increase of stress. Figure 24a-b shows the uniform strained region under SE mode and all crack outlines (light brown lines) in this region after straining to 0.6YS. Figures 24c-d show the same region and all the crack outlines in this region after straining to 0.8YS. No crack can be seen in the SE image at 0.6YS due to the low magnification. Nevertheless, cracks were observed in the SE image after straining to 0.8YS because a few cracks indicated by black arrows in Figure 24b coalesced and grew into a long and wide crack. However, the cracks indicated by blue arrows only became wider but did not show any growth in length. More cracks also initiated in the region where no crack was observed at 0.6YS when the sample was strained to 0.8YS, indicating the importance of stress in cracking.

Figure 25 shows the progression of IASCC cracks in sample B89-B1 (67.4 dpa). Two small cracks initiated at 0.5YS and the crack initiation sites were pointed out by yellow arrows. More cracks initiated in this sample at 0.6YS and these newly-initiated cracks connected, generating a long crack of hundreds of microns. The yellow arrows in Figure 25b indicate the crack initiation sites where is the widest part of the crack in a length of a grain facet. Comparing with the BSE image, we can find that crack initiation sites are correlated with triple junction and heavily localized deformation. A similar phenomenon was also observed in sample B35-B1, as shown in Figure 26. Two cracks initiated at the triple junction at 0.5YS and grew into a long crack after straining to 0.6YS.
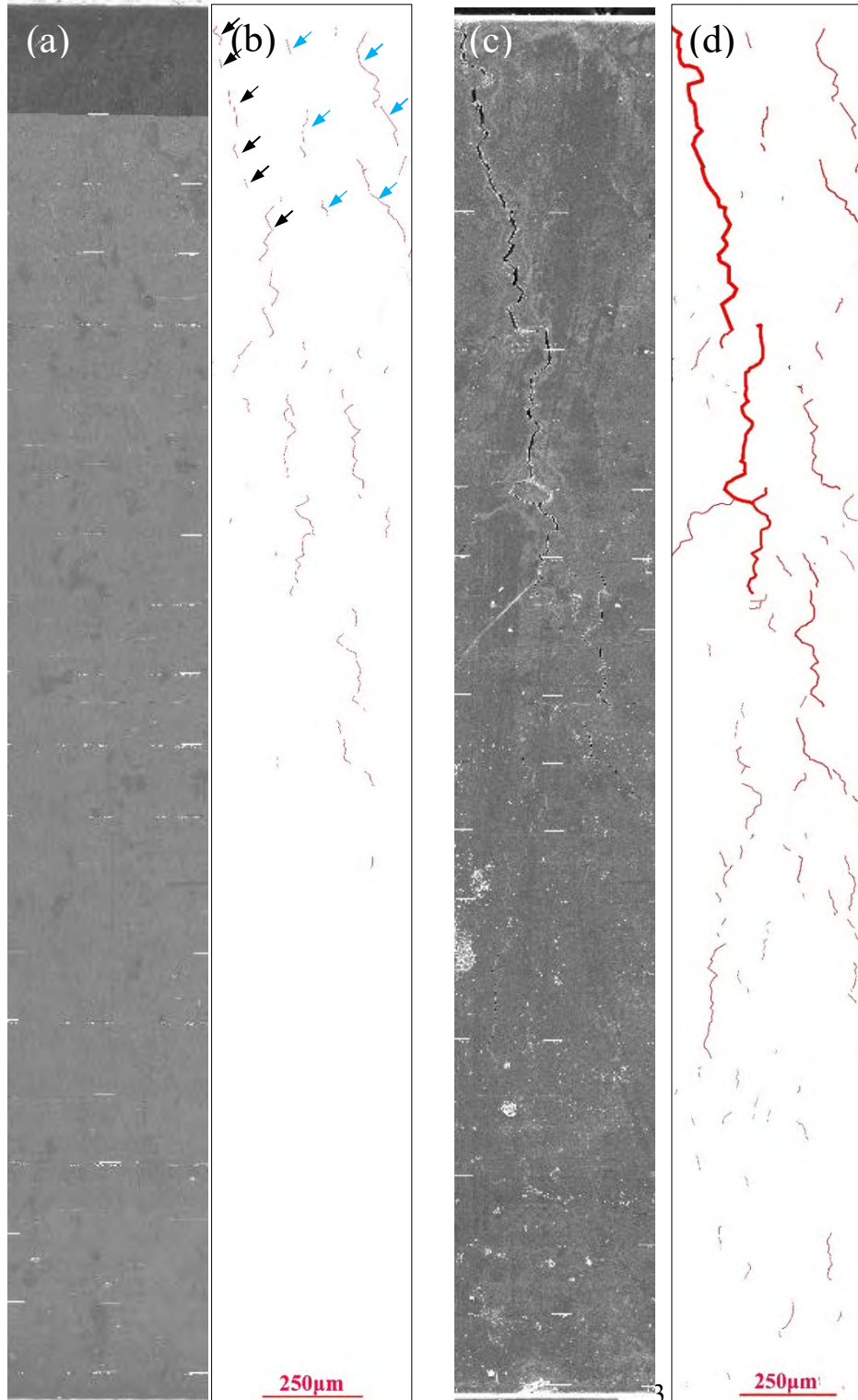
Figure 24. Cracks in the constant strain region at 0.6YS (a-b) and 0.8YS (c-d) of sample B101-B1 (46.9 dpa). Some cracks coalesced and turned into a large crack while other cracks did not grow.
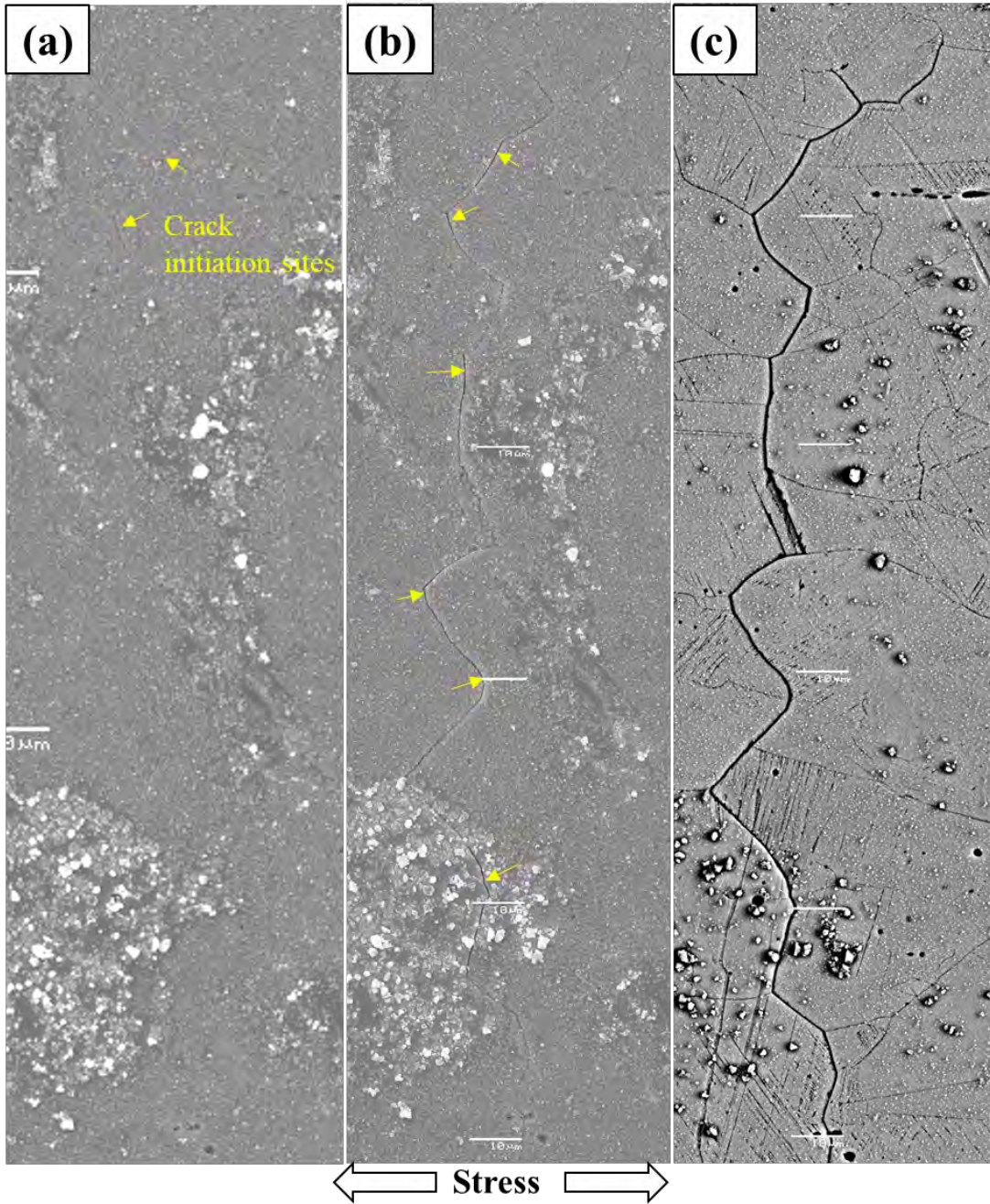
Figure 25. The development of cracks in sample B89-B1 (67.4 dpa). Two small cracks initiated at 0.5YS, as indicated by the yellow arrows (a). More cracks initiated at 0.6YS and connected, generating a long crack of hundreds of microns (b). The same crack under BSE mode (c).
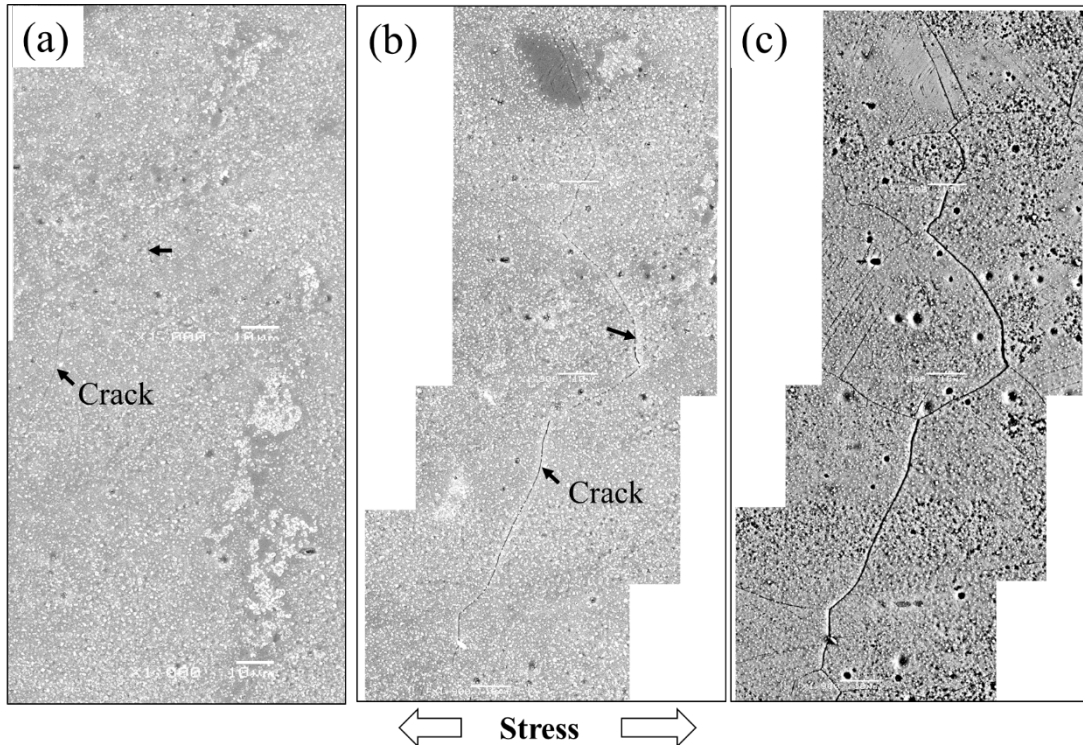
Figure 26. The development of cracks in sample B35-B1 (125.4 dpa). Two small cracks initiated at 0.5YS, as indicated by the black arrows (a). The cracks grew longer and jointed after straining to 0.6YS (b). The same crack under BSE mode (c). The crack is darker and wider than other uncracked GBs.

In summary, IG cracks initiated in the highly irradiated CW 316 SS samples at a stress level well below the yield stress. GB oxidization was observed before crack initiation in PWR primary water. A careful comparison reveals that triple junction and heavily localized deformation (LD) sites are the locations where crack initiation prefers. Long cracks in the sample were usually generated by the coalescing of multiple short cracks.

3.3.3 Characterizations of Crack

The total number and average length of the crack in the uniform strained region, as well as crack density and crack length per unit area at different stress are summarized in Table 8. From this table, it is evident that the crack number density and average length increased with stress. B101-B1 had more cracks and larger average crack length at the nominal stress of 0.6YS due to the non-uniform thickness. On the contrary, B89-B1 and B35-B1 had a comparable number and average length at the same stress level. Only one crack initiated in B35-B1 at 0.45YS and the number increased to 15 at 0.5YS, which is of the same order as B101-B1 and B89-B1. Considering the change of crack number with stress, it is possible to back extrapolate that the stress to initiate a crack in B101-B1 and B89-B1 is close to 0.45YS. The number of cracks at the lowest stress to initiation were 1 at 0.45YS (B35), 7 at 0.5YS (B89) and 72 at 0.6YS (B101). Since the 0.45YS condition was not tested in B89 and neither 0.45YS nor 0.5YS were tested in B101 it is possible that all of the samples could have initiated cracks at 0.45 YS , and then there would be no dependence on dpa.

26

Table 8. Interupted strain results of four-point bend CW 316 SS samples of various dpa.

Sample ID	Dose (dpa)	Percent of yield stress (%)	Number of cracks (#)	Average length (μm)	Number density (#/mm^2)	Length density (μm/mm^2)
B101-B1	46.9	40	0	0	0	0
		60	72	75±0.9	41.5±2	3130±79
		80	99	106.1±3.2	56.6±2	6005.2±124
B89-B1	67.4	40	0	0	0	0
		50	7	28.7±0.5	4±1.2	115.1±1
		60	43	35.5±0.8	24.6±1	860.3±37
B35-B1	125.4	40	0	0	0	0
		45	1	53.3	0.6	30.4
		50	15	28.2±1	8.6±1	241.5±25
		60	59	33.6±1	33.7±2	1134.6±49

Statistical analysis of the cracks in B89-B1 and B35-B1 showed that the majority of the cracks occurred on GBs with trace inclination greater than 50° (Figure 27), similar to the results reported by West et al. [15] and McMurtrey et al. [16]. Kamaya et al. [17] reported that the normal stress is large at GBs that are perpendicular to the load axis even though the applied load is uniform. Therefore, the GBs with favorable orientation become the preferable crack initiation sites and propagation paths. Of course, the GB inclination is not the only parameter affecting crack initiation. The GB type[18, 19], grain elastic stiffness, and orientation [20], and the value of Schmid and Taylor factors [15] have all been reported to have an impact on the IASCC cracking propensity.
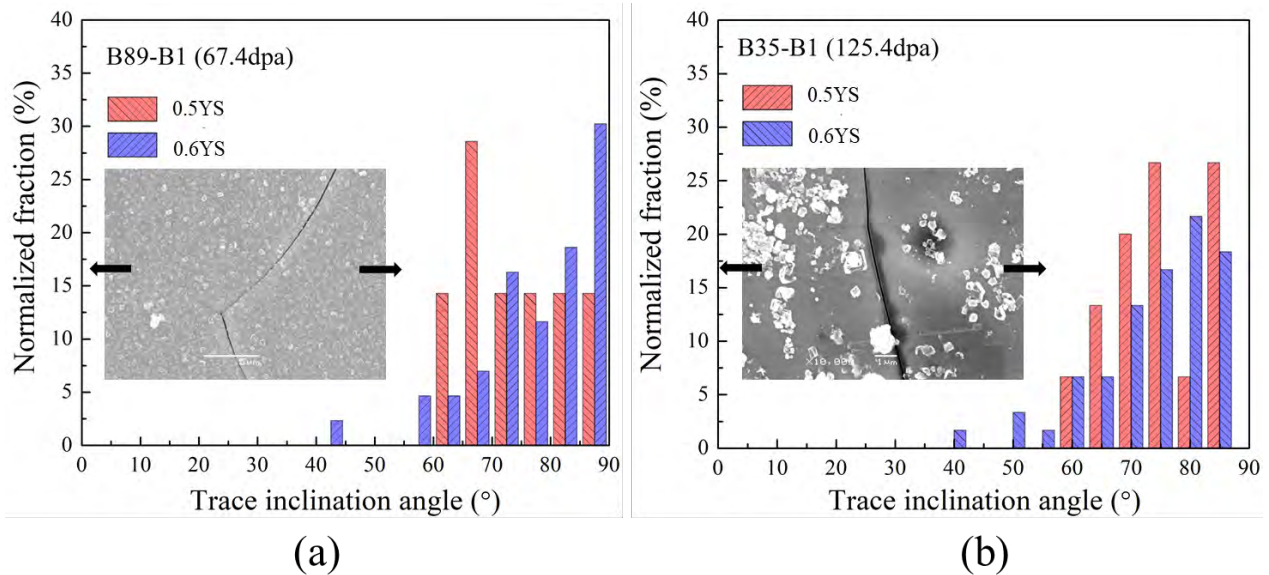
Figure 27. Distribution of the trace inclinations for IG cracks on samples B89-B1(a) and B35-B1(b).

To study the evolution of cracks with stress and their dependence on the dose, histograms were plotted in Figure 28. As shown in Figure 28a and b, the majority of the cracks are shorter than 120 μm at each

stress level and the maximum crack length increases with stress. Analysis of the crack histories revealed that some small cracks coalesced and grew into long cracks with the increase of stress. The total number of cracks did not show a rapid increase when the long crack started to grow. For example, the number of cracks in B101-B1 at 0.6YS was 72, while only 27 more cracks were generated after straining to 0.8YS. This is because the increase in stress caused the longer cracks to grow, thus relieving the stress around the cracks and suppressing the initiation of new cracks. Similar results were also reported in non-irradiated 304 SS [34]. Figure 28c shows the distribution of crack length as a function of dose at 0.6YS. The distributions of crack length among the three different doses sample are similar, except that the crack length of B101-B1is larger than the other two samples.
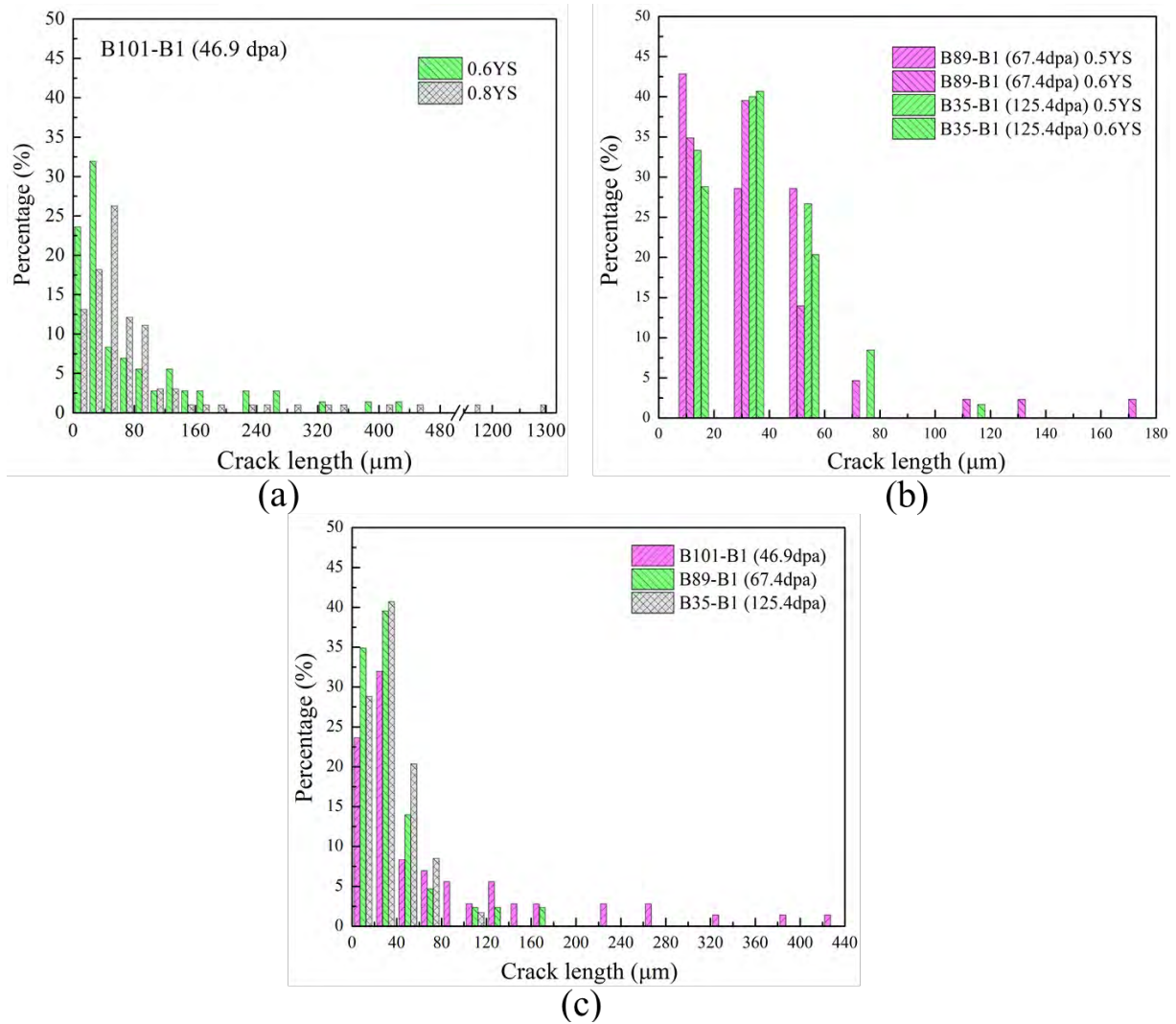
Figure 28. The distribution of crack length in (a) B101-B1, (b) B89-B1and B35-B1 at different stresses. (c) The distribution of crack length as a function of dose at 0.6YS.

3.4   Four-point Bend Test Results of SA 304 SS

This section presents the four-point bend test results from irradiated SA 304 SS samples tested by incremental loading. Load-LVDT displacement curves were provided, followed by the examination of surface and long edges of the bend sample in the uniform strained region after load increment. Cracks that initiated in the uniform strained region were fully characterized and quantified.

3.4.1   Interrupted Strain Behavior

304 SS samples were tested using the same method as CW 316 SS samples. Ex-situ characterization in the SEM was conducted following each step. Figures 29-32 show plots of load vs. LVDT displacement. Tare load imposed on the bend sample was added when the lines were plotted. From these figures, the load applied to achieve the target stress in the tensile surface was determined. A good linear relationship of load with LVDT displacement was observed.

Based on the CERT results and their yield strengths, the 5.4 dpa sample should be the least sensitive condition to cracking in high-temperature water. Therefore, to ensure that the initial stress applied to the sample is not too aggressive the sample A84-1-1 was selected as the first one to be tested. It was strained to 0.5YS and no crack appeared in the uniform strained region. The stress was then increased to 0.6YS, as shown in Figure 29. As a result, five cracks initiated in the uniform strained region. To study how the crack develops with load the sample was further strained to 0.7YS. More cracks were generated in the sample after straining to 0.7YS. The crack length, maximum width, and the trace inclination to load axis were measured.

A32-1-1 was selected as the second sample to be tested as it was supposed to be the most sensitive material to cracking in high-temperature water. Figure 30 shows the load vs. LVDT displacement response of sample A31-1-1. The stress given in the plot was corrected considering the thickness. Given the high IASCC susceptibility of 125.4 dpa sample, it was strained to 0.35YS for the first step. However, no cracks were observed in the uniform strained region until 0.79YS. Three cracks initiated in the sample after staining to 0.79YS. Characterization of each crack was conducted using the SEM. The results from the 5.4 and 125.4 dpa samples were used to determine the amount of stress to be be applied to the other two samples.

Figure 31 shows the interrupted strain results of A98-1-2. As we have known that the minimum stress to initiate a crack in 304 SS samples is 0.6YS, the 69 dpa sample was strained to 0.5YS for the first step. Surprisingly, this sample did not crack until the stress was increased to 0.8YS. Seven cracks in the uniform strained region were generated. Considering that 69 and 125.4 dpa samples cracked at ~0.8YS, the 95 dpa sample was strained to 0.6YS for the first step. However, 16 cracks were observed after the test. With the progress of the experiment and the characterization of cracks generated in bend samples, we realized that GB oxidization is of great importance in the process of crack initiation. GB oxidization is closely related to the exposure time in high-temperature water. Hence, to verify our thoughts this sample was strained again to 0.6YS using the same procedure, as shown in Figure 32. As a result, 10 more cracks were generated in the sample.
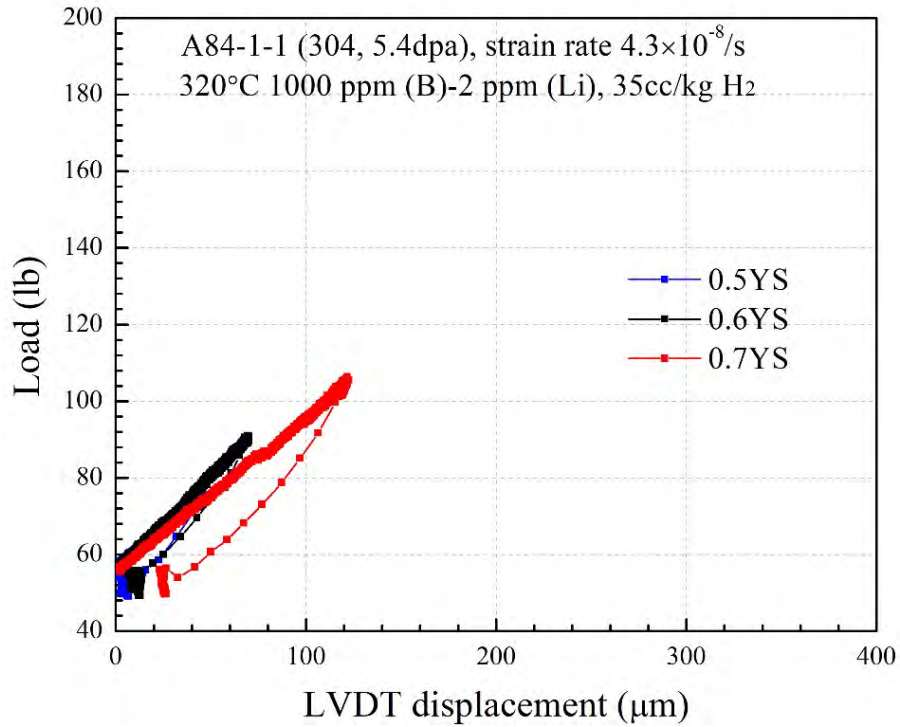
Figure 29. Load vs LVDT displacement for the sample A84-1-1 (5.4 dpa) in primary water. Cracks in the sample were observed after straining to 60% of the irradiated yield strength.
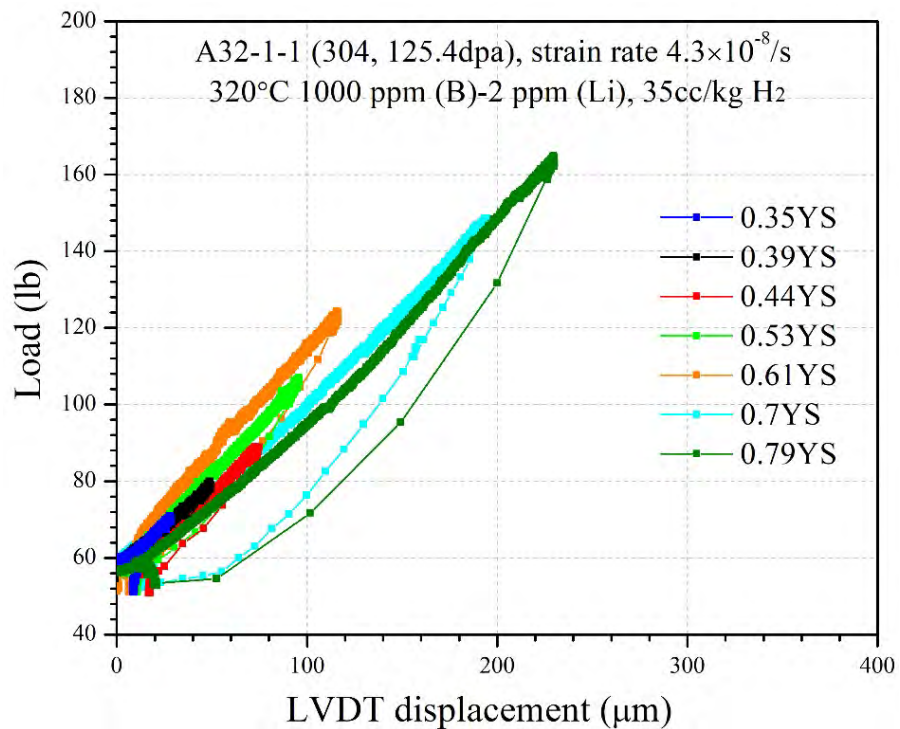
Figure 30. Load vs LVDT displacement for the sample A32-1-1 (125.4 dpa) in primary water. Cracks in the sample were observed after straining to 79% of the irradiated yield strength.
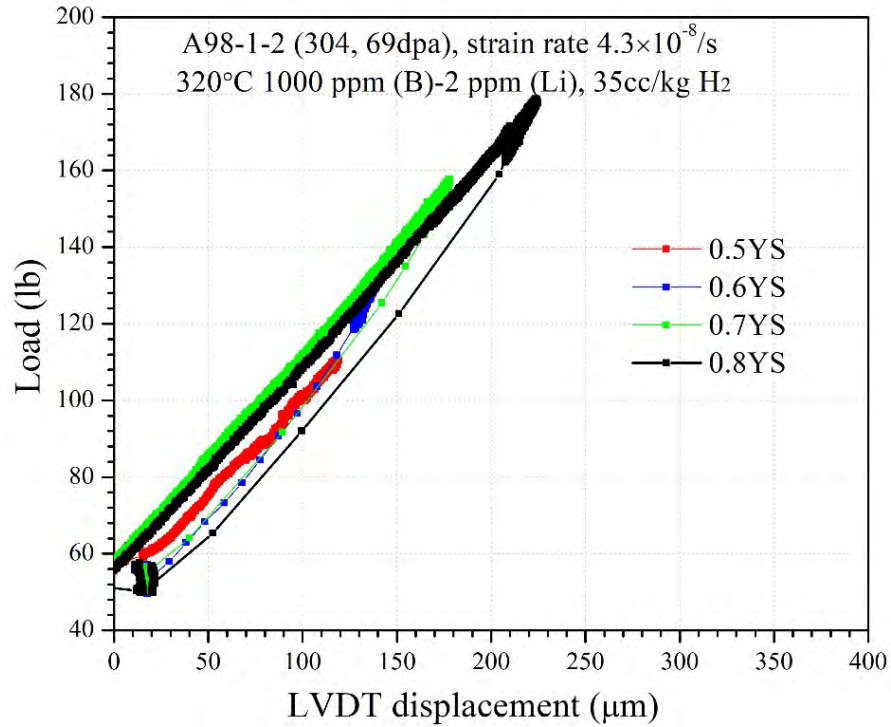
Figure 31. Load vs LVDT displacement for the sample A98-1-2 (69 dpa) in primary water. Cracks in the sample were observed after straining to 80% of the irradiated yield strength.
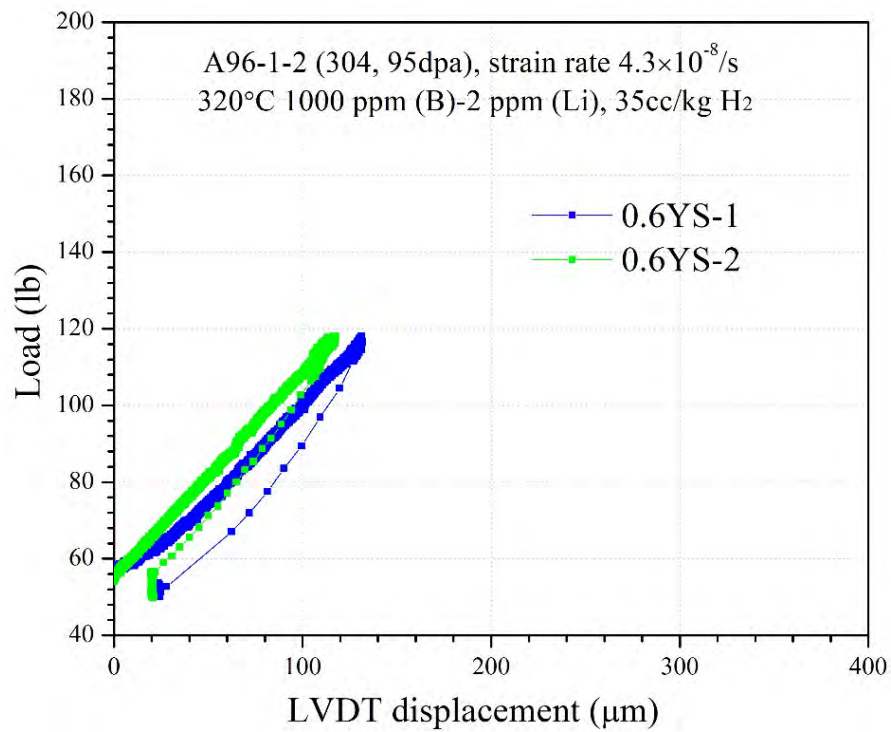
Figure 32. Load vs LVDT displacement for the sample A96-1-2 (95 dpa) in primary water. Cracks in the sample were observed after straining to 60% of the irradiated yield strength.

Figure 33 shows the morphology of four-point bend samples after the last strain test. Yellow dashed lines outlined the uniform strained region in each sample. From the supporting marks (dark regions) on the sample, we can conclude that all the samples were centered well and loaded symmetrically.
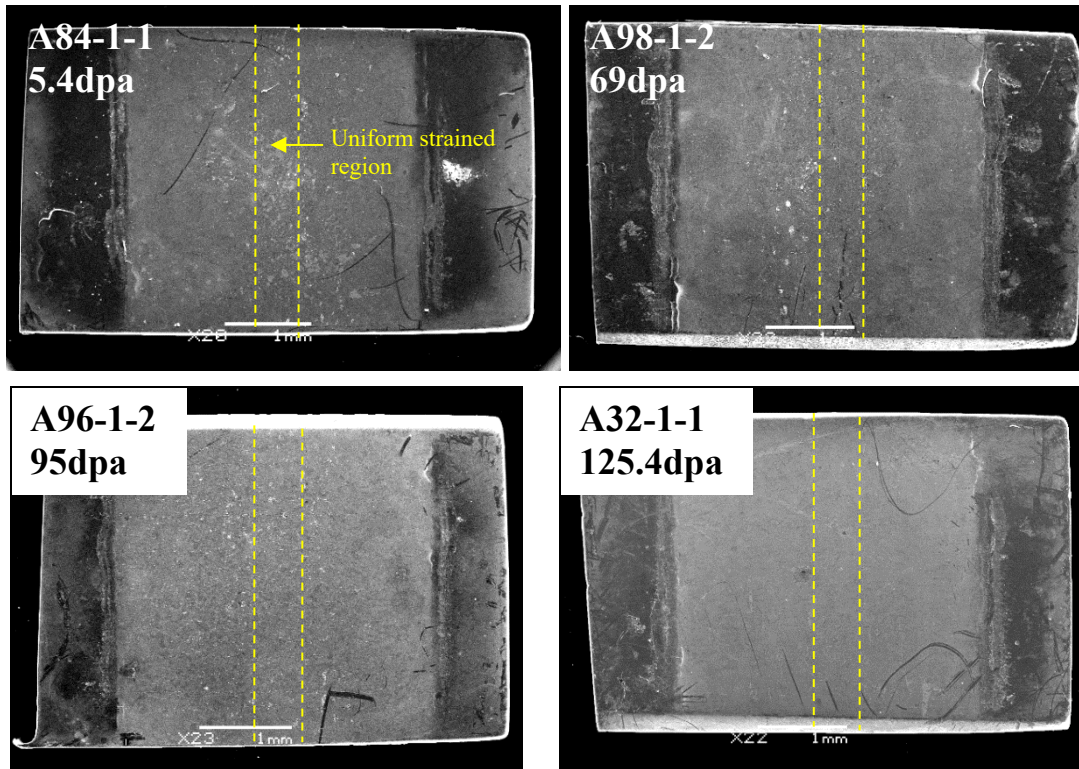
Figure 33. The morphology of four-point bend samples after the completion of the test.

3.4.2 Crack Initiation and Propagation

All the 304 SS bend samples cracked at a stress level below their irradiated yield strengths, as summarized in Table 9. Crack even initiated at 60% of the irradiated yield strength in 5.4 and 95 dpa samples. Figure 34 shows the representative cracks that appeared at a time when the crack initiation was observed for the first time.

Table 9. Crack initiation stress for the SA 304 SS samples.

Sample ID	Dose (dpa)	Initiation stress (% of YS)
A84-1-1	5.4	60
A98-1-2	69	80
A96-1-2	95	60
A32-1-1	125.4	79
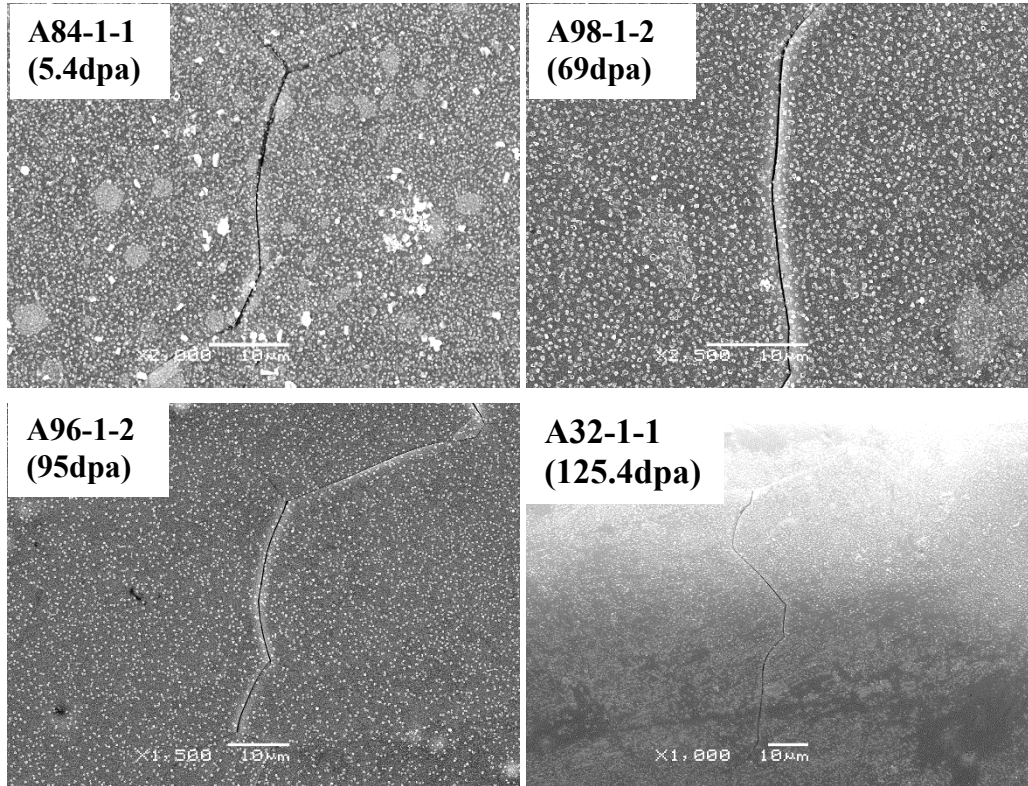
Figure 34. Representative cracks in 304 SS samples when the crack initiation was observed for the first time.

Tables 10-12 present the evolution of GBs with increase of stress in 5.4, 69, and 125.4 dpa samples, respectively. The condition of each GB, the occurrence of DC, the length of crack and suspect crack, and the number of DC intersecting crack/GB were recorded after each step. Table 10 shows the evolution of GBs in sample A84-1-1 (5.4 dpa). Thirty-two GBs were traced in the period of the test. Some of the GBs were oxidized after straining to 0.5YS while some GBs were not. No crack initiated at this stress level yet but a DC was generated. The fraction of GB intersected by DC was calculated to be 3.1%. Five cracks and six suspect cracks initiated in the sample when it was strained to 0.6YS. 80% percent of cracks and 67% percent of suspect cracks were developed from oxidized GBs. The number of DCs increased rapidly and 68.8% percent of the traced GBs were intersected by DCs after straining to 0.6YS. For the cracks and suspected cracks, the fraction was even higher. More cracks and suspected cracks were generated when the sample was strained to 0.7YS. Some cracks were developed from suspected cracks while the remaining ones developed from oxidized GBs. The number of DC increased with stress and 90.6% percent of the traced GBs were intersected by DCs at 0.7YS. Comparing the number of DCs at different stresses, the number of DCs nearby GBs did not show a significant increase with stress.

The development history of GBs in samples A98-1-2 and A32-1-1 was very similar to that in sample A84-1-1. Cracks and suspected cracks developed from oxidized GB. A small amount of DCs appeared at low-stress level and increased rapidly with stress. The majority of the crack and suspect crack are intersected by DCs. Besides, we also find that the earlier DCs appear the earlier crack can initiate, indicating that DCs are accelerating the initiation of crack.

Table 10. Record of the evolution of GBs with stress in sample A84-1-1 (5.4 dpa)

ID of image	ID of GB/crack	Condition			Crack length (um)		Number of DC intersecting crack/GB		
		0.5YS	0.6YS	0.7YS	0.6YS	0.7YS	0.5YS	0.6YS	0.7YS
24x6	1	⊗	√*	√*	38.8	38.8	0	4	4
26x2	2	⊗	√*	√*	121.7	121.7	0	4	6
26x4	3	⊗	√*	√*	116.3	151.5	0	5	7
33x4	4	⊗	√*	√*	3.9	3.9	0	1	2
34x4	5	×	√*	√*	9.8	10.3	0	3	4
23x6	6	⊗	O*	√*	46.8	85.4	0	4	4
25x5	7	⊗	O *	√*	72.3	104.4	0	4	4
29x6	8	×	O *	√*	52.4	71.8	0	5	6
35x5	9	×	O *	√*	56.7	120.4	0	3	5
16x2	10	⊗	⊗	√*	-	72.4	0	0	1
31x6	11	×	⊗*	√*	-	93.9	0	1	1
19x5	12	⊗	⊗*	√*	-	68.0	0	2	4
20x6	13	×	⊗	√	-	14.1	0	0	0
23x3	14	×	⊗*	√*	-	60.9	0	1	1
29x1	15	⊗	⊗*	√*	-	50.5	0	1	1
36x5	16	×	⊗	√*	-	20.0	0	0	1
28x4	17	⊗	⊗*	√*	-	116.1	0	3	4
23x4	18	⊗	O	O	23.7	23.7	0	0	0
40x4	19	⊗	O *	O *	30	30	0	1	3
28x7	20	×	⊗*	O *	-	47.2	0	2	2
33x5	21	⊗	⊗*	O *	-	22	0	1	1
2x7	22	×	⊗	O *	-	27.4	0	0	1
6x5	23	⊗	⊗	O *	-	37.6	0	0	1
13x4	24	⊗	⊗*	O *	-	78.3	0	6	6
14x5	25	×	⊗	O	-	65.2	0	0	0
18x3	26	×	⊗	O *	-	43.6	0	0	2
19x3	27	⊗*	⊗*	O *	-	51.8	1	2	2
20x2	28	⊗	⊗	O *	-	78.1	0	0	4
27x4	29	×	⊗*	O *	-	23.5	0	4	5
31x7	30	×	⊗	O *	-	50	0	0	1
32x6	31	×	⊗*	O *	-	26.7	0	1	2
34x7	32	×	⊗*	⊗*	-		0	1	1
Total number of crack		0	5	17	-	-	-	-	-
Fraction of GB/crack with DCs		3.1%	68.8%	90.6%	-	-	-	-	-

Note: ×- Intact GB, ⊗- Oxidized GB, O- Suspected crack, √-Cracked, *- Occurrence of DCs intersecting crack or GB

▪ Crack initiation at 0.6YS	▪ Crack initiation at 0.7YS	
▪ Suspected crack at 0.7YS	▪ Oxidized GB at 0.7YS	

Table 11. Record of the evolution of GBs with stress in sample A98-1-2 (69 dpa)

ID of image	ID of GB/crack	Condition			Crack length (um)		Number of DC intersecting crack/GB		
		0.6YS	0.7YS	0.8YS	0.7YS	0.8YS	0.6YS	0.7YS	0.8YS
9x3	1	⊗	⊗*	√*	-	47.8	0	1	3
14x5-1	2	⊗	⊗*	√*	-	24.7	0	2	5
15x4	3	⊗	⊗	√*	-	135.8	0	0	8
16x5	4	×	⊗*	√*	-	6.6	0	1	2
19x5	5	⊗*	⊗*	√*	-	38.2	2	2	4
19x6-1	6	×	⊗	√*	-	5.7	0	0	7
19x6-2	7	⊗	⊗	√*	-	15.2	0	0	4
8x5	8	⊗	⊗	O *	-	2.9	0	0	1
14x5-2	9	×	⊗*	O *	-	10.4	0	1	2
17x5-1	10	⊗	⊗*	O *	-	57.2	0	1	2
17x5-2	11	⊗	⊗*	O *	-	14.3	0	1	3
18x6	12	⊗	⊗	O *	-	70.1	0	0	7
Total number of crack		0	0	7					
Fraction of GB/crack with DCs		8.30%	58.30%	100%					

Note: ×- Intact GB, ⊗- Oxidized GB, O- Suspected crack, √-Cracked, *- Occurrence of DCs intersecting crack or GB

☐ Crack initiation at 0.8YS   ☐ Suspected crack initiation at 0.8YS

Table 12. Record of the evolution of GBs with stress in sample A32-1-1 (125.4 dpa)

ID of image	ID of GB/crack	Condition			Crack length (um)		Number of DC intersecting crack/GB		
		0.61YS	0.7YS	0.79YS	0.7YS	0.79YS	0.61YS	0.7YS	0.79YS
23x3	1	⊗	⊗	√*	-	16	0	0	1
27x4	2	⊗	⊗*	√*	-	64	0	2	4
39x5	3	⊗	⊗*	√*	-	9.2	0	1	1
1x3-3	4	⊗	O*	O*	92.5	92.5	0	3	4
39x4	5	⊗*	O*	O*	11.6	11.6	4	4	4
1x6	6	×	⊗	O*	-	8.3	0	0	1
19x5	7	⊗	⊗*	O*	-	46.3	0	1	2
21x5	8	⊗	⊗*	O*	-	38.7	0	2	3
23x5	9	⊗	⊗*	O*	-	28.4	0	1	2
25x6	10	⊗	⊗*	O*	-	22.7	0	1	2
28x6	11	×	⊗	O*	-	38.2	0	0	4
31x7	12	⊗	⊗	O	-	46.5	0	0	0
Total number of crack		0	0	3					
Fraction of GB/crack with DCs		8.30%	67%	91.60%					

Note: ×- Intact GB,⊗- Oxidized GB, O- Suspected crack, √-Cracked, *- Occurrence of DCs intersecting crack or GB

Crack initiation at 0.79YS   Crack initiation at 0.79YS

Figures 35-36 show an evolution of cracks with stress and exposure duration in the 5.4 and 69 dpa samples. Both BSE and SE images were provided in the figure. DCs generated in the sample at low stress were usually very faint and invisible under SE while very clear under BSE by virtue of the thin oxide film formed on the surface. As shown in Figure 35, no DC was observed in the image at 0.5YS. However, several DCs were generated at 0.6YS and a tight crack appeared in the SE image. The DC terminated at the GB is believed to have facilitated cracking of the GB. Though we did not see the oxidized state of the GB before crack initiation, it is still possible that the GB oxidized in the period of the test and cracked due to the high local stress generated by DC. With the increase of stress, more DCs were generated and the crack also became wider and longer.

Figure 36 shows another representative crack in 69 dpa sample. A DC intersecting the GB can be seen in the BSE image at 0.7YS. The GB stands out from surrounding GBs as darker and wider as a result of oxidization, as shown in the SE image. The GB cracked after straining to 0.8YS and more DCs were also generated. A more closet observation reveals two DCs intersecting the GB, which caused stress concentration and the subsequent cracking of the oxidized GB.
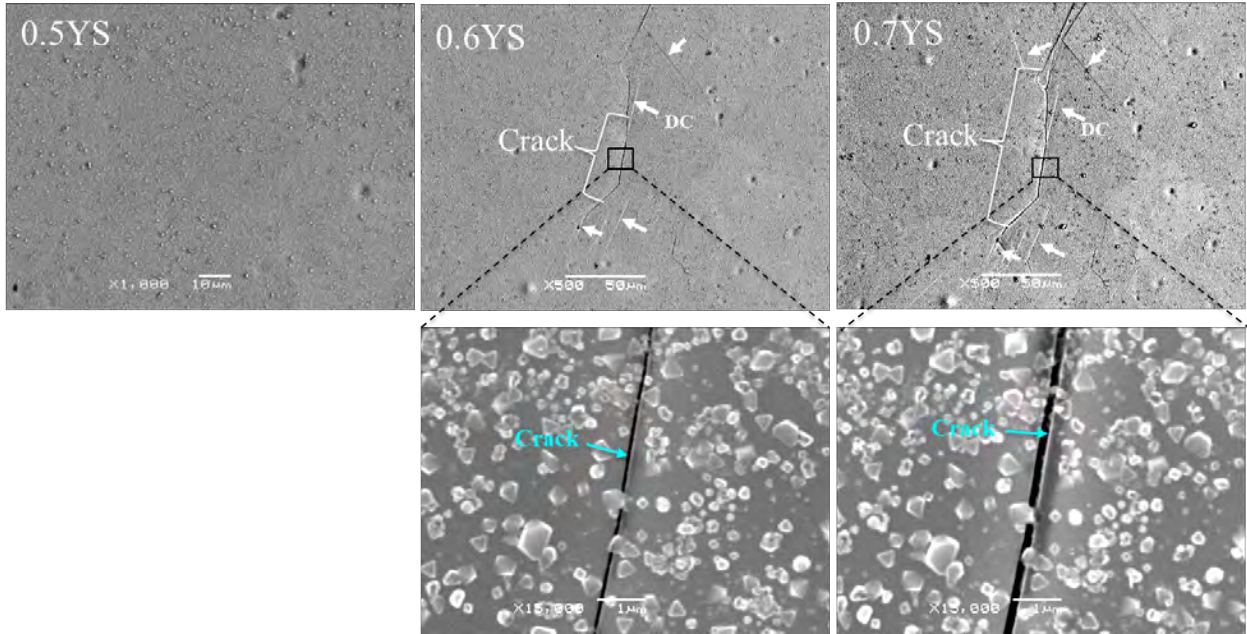
Figure 35. Evolution of a crack with stress and exposure duration in sample A84-1-1(5.4 dpa).
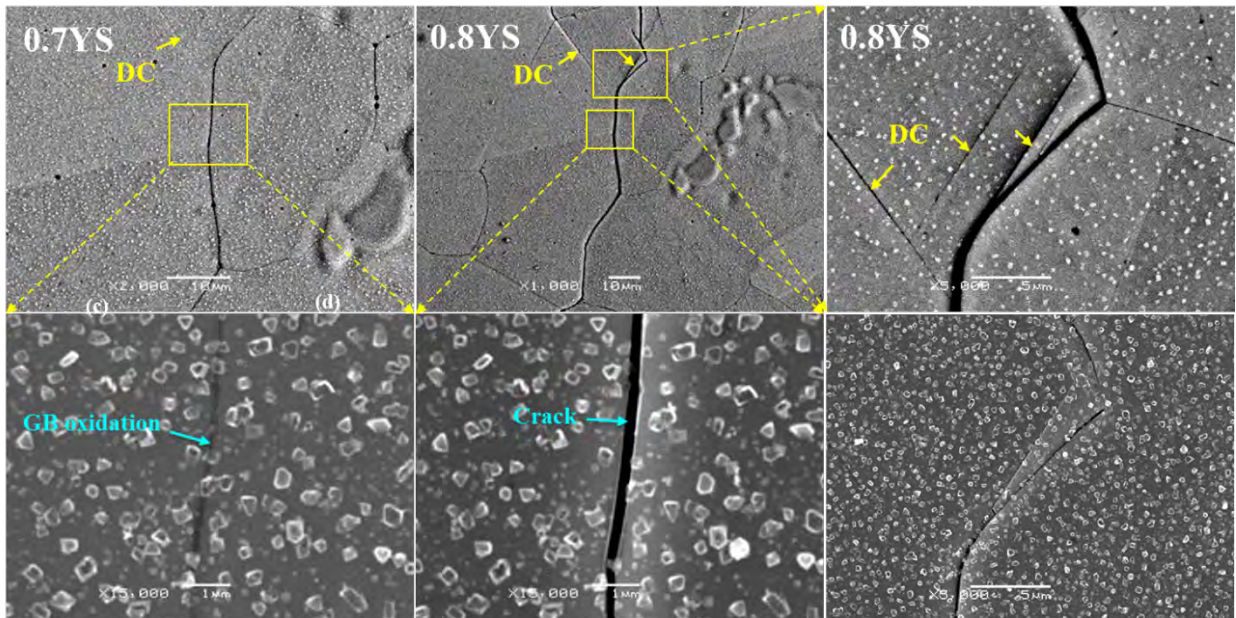
Figure 36. Evolution of a crack with stress and exposure duration in sample A98-1-2 (69 dpa)

From the results it is apparent that DCs appeared either before or concurrent with cracking. As a final condition, nearly all the cracks and suspected cracks were intersected by DCs. It still remains to be proved that uncracked GBs are not or rarely intersected by DCs compared to the cracked GBs. To verify this supposition, four uncracked GBs with similar orientation and length to a crack/suspected crack were selected randomly in the nearby. As shown in Figure 37, a crack with DCs located in the center of the picture. Four uncracked GBs, as indicated by the yellow dashed lines, were selected for analysis. The results are summarized in Tables 13-14.

Table 13 shows the results of sample A84-1-1 (5.4 dpa). Five cracks and six suspect cracks and accordingly 44 uncracked GBs were analyzed at 0.6YS. As a result, only 12.6% percent of the uncracked GB was intersected by DCs, however, a much higher fraction of suspected cracks and verified cracks were intersected by DCs; 83% percent for suspected crack and 100% percent for verified cracks. More suspected cracks and cracks were analyzed at 0.7YS. The trend for the fraction of cracked, suspected cracks, and uncracked GB with DCs did not show any change. However, the fraction of uncracked GB with DCs increased a little bit with the increase of stress. Table 14 shows the results of sample A32-1-1 (125.4dpa). This sample presents a very similar result to the 5.4 dpa sample. The uncracked GB with DCs only accounts for 29.1% percent of the total GB, while the suspected cracks and cracks account for 77.8% and 100% percent of their type.
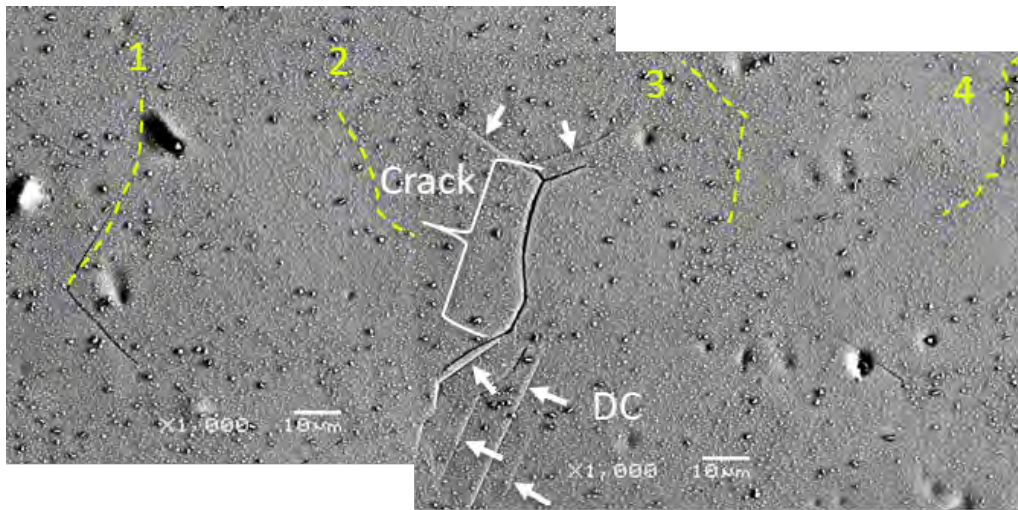
Figure 37. A stitched BSE picture showing a crack and the uncracked GBs for the analysis of the correlation of cracking with DCs.

Table 13. The correlation of crack, suspect crack, and uncracked GB with DCs in sample A84-1-1 (5.4 dpa).

Parameters	Number analyzed		Number with DC		Fraction with DC	
Stress level	0.6YS	0.7YS	0.6YS	0.7YS	0.6YS	0.7YS
Cracked	5	17	5	16	100%	94.1%
Suspected cracks	6	14	5	12	83%	85.7%
Uncracked GB	44	124	7	26	15.9%	20.9%

Table 14. The correlation of cracked, suspected cracks, and uncracked GB with DCs in sample A32-1-1 (125.4 dpa).

GB/crack	Number of the analyzed object	Number of the object with DC	The fraction of the object with DC
Stress level	0.79YS	0.79YS	0.79YS
Cracked	3	3	100%
Suspected cracks	9	7	77.8%
Uncracked GB	48	14	29.1%

Figure 38 shows the development of a GB in sample A96-1-2 (95 dpa) after straining to 0.6YS twice. Figure 38c, shows a GB that was oxidized after staining to 0.6YS for the first time. However, it developed into a crack when it was strained to 0.6YS for the second time, suggesting that stress is not the only factor affecting crack initiation. Because the uncracked GB that has been through the same stress condition should not crack if the stress was the only factor. Due to the same procedure used for the second time, the increased exposure time to high-temperature water was the only additional parameter that could affect crack initiation. Longer exposure time enhanced the corrosion process of material and of course the oxidization of GB. This result agrees well with the evolution of a crack: the oxidization of GB, the formation of DC, and then cracking. Kale et al. [5] also reported that the neutron-irradiated sample did not crack in the high-temperature Ar though the applied stress was above the stress threshold. Figure 39 shows the development of a crack in sample A96-1-2 (95 dpa) after straining to 0.6YS twice. The width of the crack also increased from 165nm to 385nm.
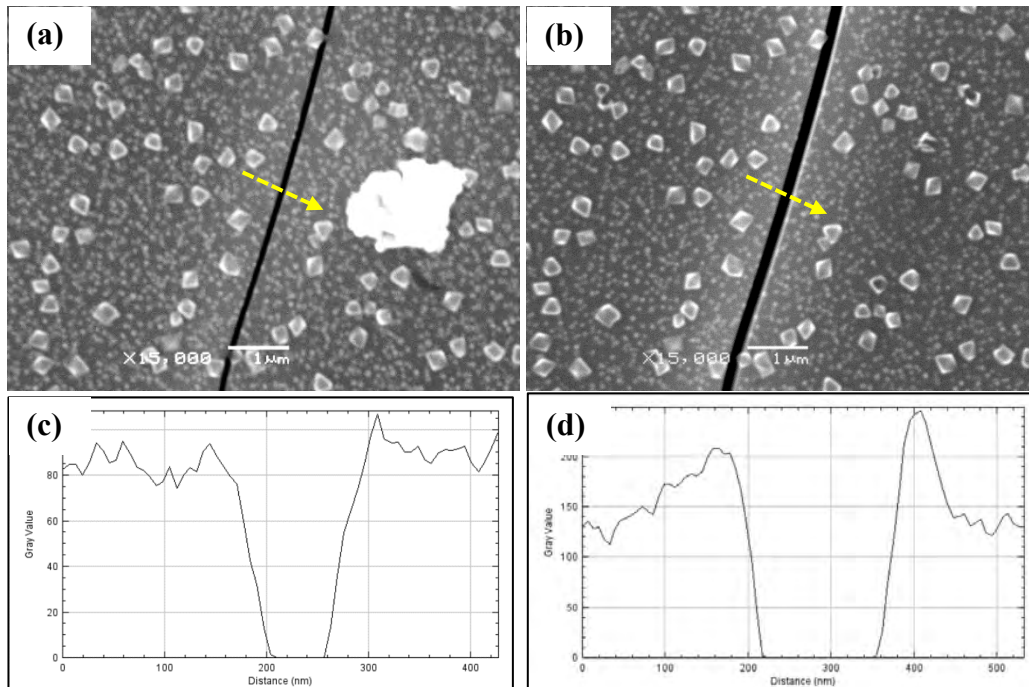
Figure 38.The development of oxidized GB (a) to a crack (b) in sample A96-1-2 (95 dpa) after straining it to 0.6YS again. (c) and (d) are the gray value plots over the GB and crack.
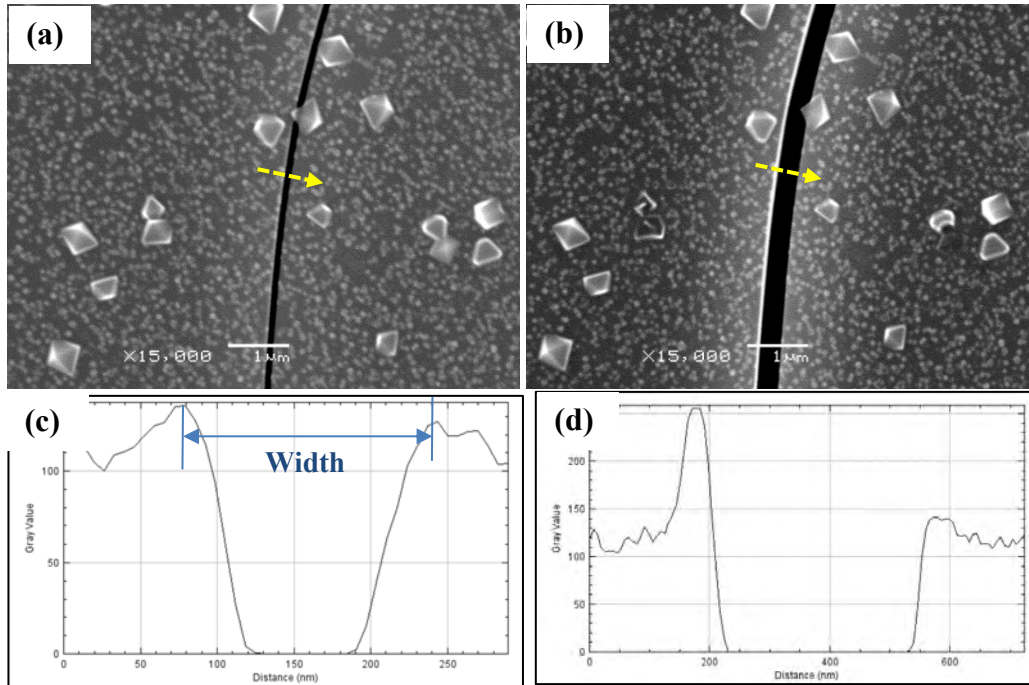
Figure 39. A small crack (a) becomes a wider crack (b) in sample A96-1-2 (95 dpa) after straining it to 0.6YS again. (c) and (d) are the gray value plots over the crack.

3.4.3 Characterization of Cracks

The total number and average length of the crack in the uniform strained region, as well as crack density and crack length per unit at different stress are summarized in Table 15. The 5.4 and 95 dpa samples initiated crack at 0.6YS, while the 69 and 125.4 dpa samples initiated crack at 0.8YS. The difference in the crack initiation stress is not related to dpa. It could be attributed to the intrinsic data scatter. From this table, we can find that crack number and average length increases with stress and exposure duration. A96-1-2 has more cracks and larger average crack length when the crack initiation was observed for the first time, which might result from the uninterrupted straining step. The oxidization process of GB was not disturbed during the test and the dynamic strain continually promoted the GB degradation process, which gave the oxidized GB more chance to cracking. Therefore, more cracks will be generated when the threshold stress was achieved. On the contrast, the number of the crack in the other three samples was of the same order and the average length was comparable when crack initiation was observed for the first time.

Figure 40 presents the location of each crack in the uniform strained region. The space between two dashed lines is a uniform strained region. The short lines are cracks facsimiled from their corresponding physical sample. As shown in the schematic diagrams, cracks are evenly distributed in the uniform strained region and no crack outside of this region can be found. No crack initiated on the long edges of the sample, suggesting that the sample was strained evenly along the short axis.

Table 15. Interrupted strain results of four-point bend 304 SS samples of various dpa.

Sample ID	Dose (dpa)	Percent of yield stress (%)	Number of cracks (#)	Average length (μm)	Number density (#/mm^2)	Length density (μm/mm^2)
A84-1-1	5.4	50	0	0	0	0
		60	5	58.1±1.7	2.9	166±39.3
		70	17	62.8±2.3	9.7	610.2±47.5
A98-1-2	69	50	0	0	0	0
		60	0	0	0	0
		70	0	0	0	0
		80	7	39.2±2.1	4	156±42.6
A96-1-2	95	60	16	76.4±2.2	9.1	698.5
		60	26	157±3.4	14.8	2333±61.4
A32-1-1	125.4	35	0	0	0	0
		39	0	0	0	0
		44	0	0	0	0
		53	0	0	0	0
		61	0	0	0	0
		70	0	0	0	0
		79	3	29.7±1.5	1.7	50.9±18.6
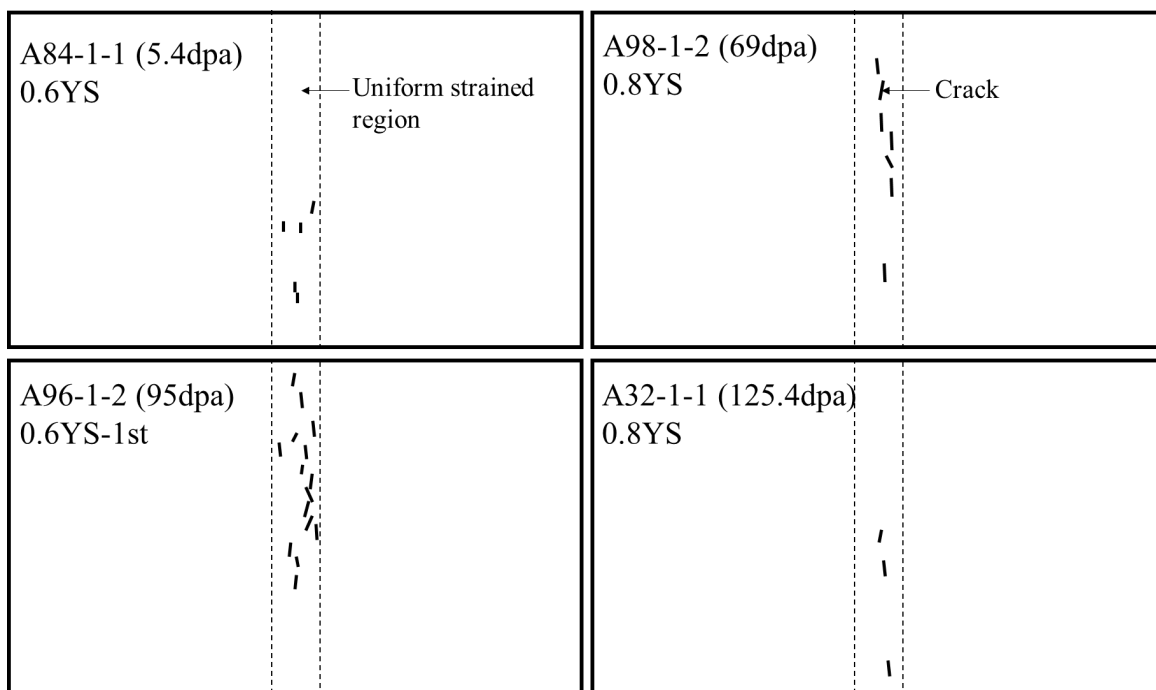
Figure 40. Distribution of cracks in the uniform strained region following application of the stress to initiate cracking.

Statistical analysis of the cracks in 304 SS samples showed that the majority of the cracks occurred on GBs with trace inclination greater than 60° (Figure 41), which is similar to the result of CW 316 SS samples,

indicating the importance of normal stress in crack initiation. Furthermore, it seems that the fraction of cracks with high trace inclination is higher if the 125.4 dpa sample was excluded, as only three cracks initiated in that sample. The normal stress dependence of the cracking may either be a result of a higher propensity for IG crack nucleation on highly stressed surfaces, or the greater propensity for IG cracks to grow along boundaries experiencing high normal stresses
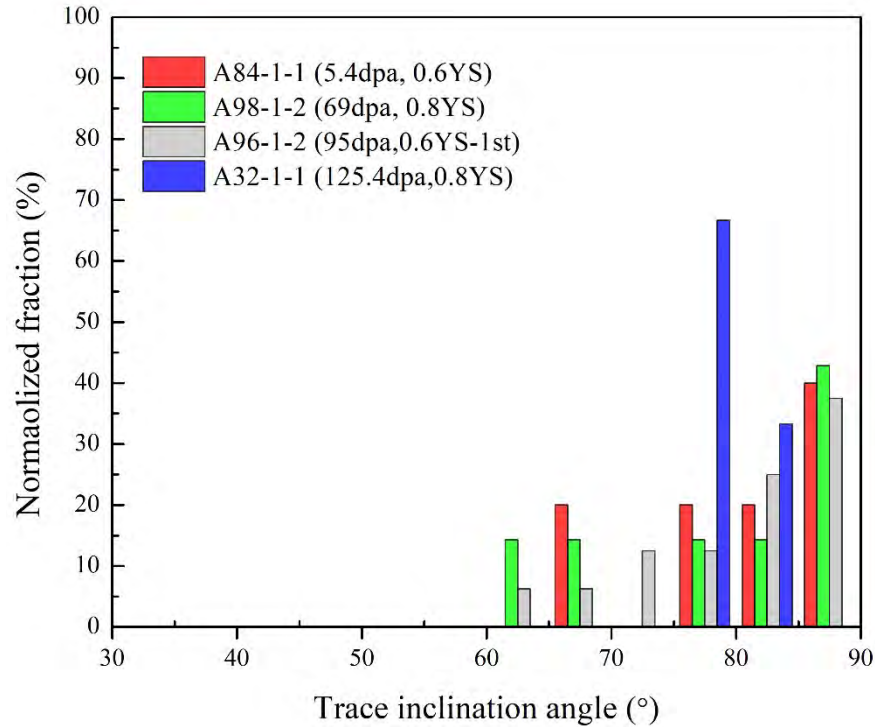
Figure 41 Distribution of the trace inclinations for IG cracks in 304 SS samples, when crack initiation was observed for the first time.

To directly compare the cracks among samples and study their dependence on the dose, the length and width of every single crack were plotted in Figure 42. Note that the ID number of the crack in Figure 42a and Figure 42b does not correspond to the same crack. They were simply ranked by the size of length and width for a better display. The distribution of crack length shows a larger variation than crack width. The smallest length of a crack is a few microns while the largest size could be ~ 220 μm. However, the crack width only ranges from 140 to 270 nm. For now, 140 nm seems to be the resolution limit of our SEM to differentiate a crack. From this figure, we can find that the sample with the most cracks also shows the largest crack length and width. This could be attributed to the growth of crack after initiation. A better explanation is given in Figure 43. This figure shows the distribution of length and width of cracks in sample A96-1-2 (95 dpa) after straining to 0.6YS twice. Crack number, the largest crack length, and the maximum crack width increased from 16 to 26, 220 to 550 μm, and 270 to 380 nm, respectively, after the second straining.
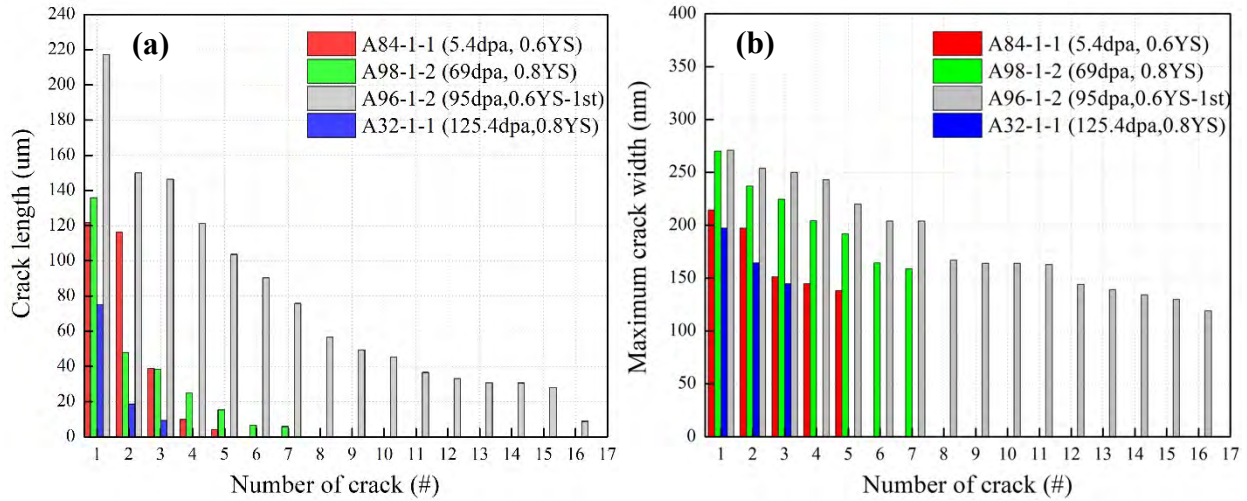
Figure 42. Length (a) and the maximum width (b) of cracks in the four different dpa samples
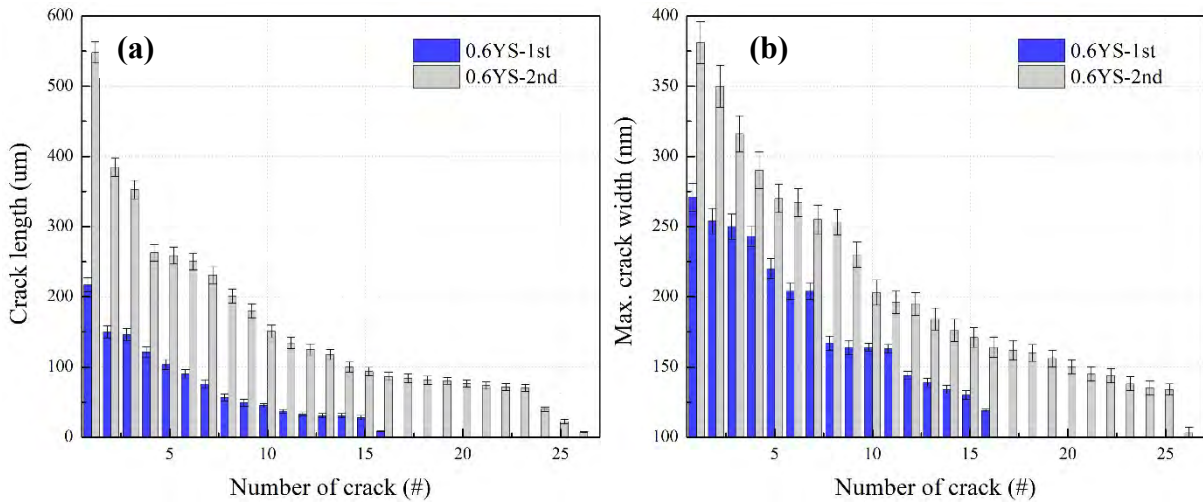
Figure 43. Length (a) and the maximum width (b) of cracks in the 95 dpa sample after straining to 0.6YS twice.

4. DISCUSSION

To better understand the crack initiation behavior in irradiated austenitic stainless steels, the discussion section of this report is divided into the following three sections: irradiated microstructure, oxidization and localized deformation on IASCC, and IASCC stress threshold.

4.1 Irradiated Microstructure

Neutron irradiation at temperatures close to 330°C induces Frank loops, precipitates and segregation. The evolution of the density and average diameter of loops and precipitates measured in CW 316 SS as well as the data from reference [9] of the same heat are plotted in Figure 44. Loop size and density saturates by ~ 10 dpa and remains unchanged up to 125.4 dpa. As for precipitates, the density decreased with dose

up to about 40 dpa after which it reached a relatively stable value of ~3.5×10^{21} m^{-3}. Correspondingly, the size of precipitates increased with dose and stabilized at about 8-10 nm. Cavities were not detected, which could be attributed to the relatively low irradiation temperature. Loops, and precipitates lead to irradiation hardening of materials and consequently the increase of yield strength, with loops being the dominating factors[21, 22]. The stable size and density of loops and precipitates at higher doses indicate that the hardness and yield strength have reached a stable state, which agrees well with our measured hardness and yield strength (Table 4). Hardness and yield strength have been associated with SCC susceptibility of irradiated materials, which in this case is consistent with the observed IASCC behavior in that neither quantity changes across the dose range examined here.
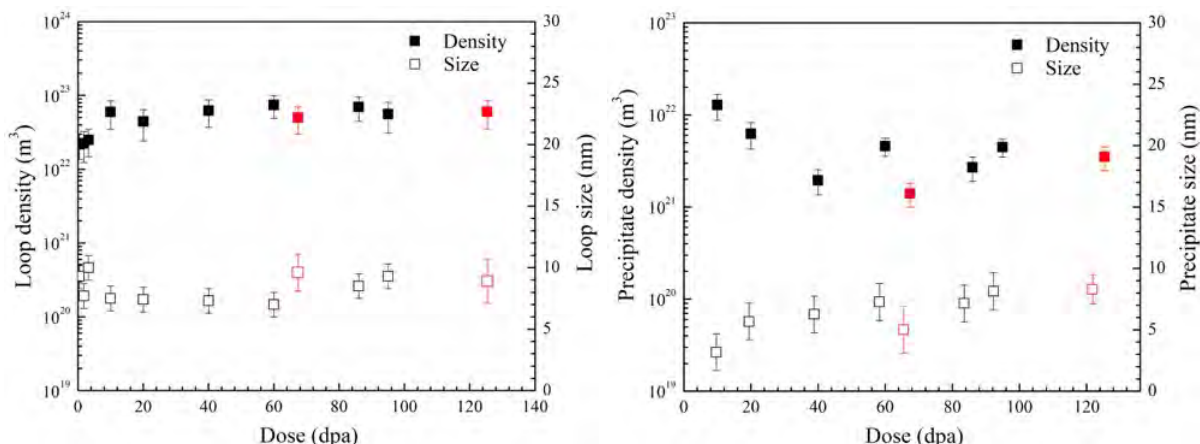
Figure 44. Density and size of (a) loops and (b) precipitates as a function of dose in the CW 316 SS. The data in black are from the reference **[9]** and the data in red are from this work.

4.2   GB Oxidization and Localized deformation on IASCC

IASCC is a complex phenomenon in which material properties, stress and water chemistry are simultaneously changed by irradiation and its mechanisms are not yet well understood. Recent studies have focused on the combination of high local stress/strain concentration at GB caused by heterogeneous deformation [13, 21, 23] and degradation of GB binding strength due to various factors. One such factor is considered to be GB oxidation [24].

4.2.1   CW 316 SS

Figure 45 shows a representative crack developing in sample B35-B1 with increasing stress and exposure time. This sample experienced four incremental stress conditions; 0.4YS, 0.45YS, 0.5YS, and 0.6YS. The total exposure time at stress, adding up all the individual steps is around 320 hours. Similarly, the total exposure times for B101-B1 and B89-B1 were 354.2 and 318.7 hours, respectively.

Figure 45a shows the morphology of the crack initiation site before exposure, which is free of scratches and contamination. The round back dots with white circles are likely MnS inclusions which match those found in the TEM analysis of the inclusions of similar shape and size. These MnS inclusions are all in the grain interior, as shown in Figure 45h. The analyses of many cracks confirmed that they rarely initiate at MnS inclusions. Thus, the MnS inclusions are not perceived to be responsible for the crack initiation in

most cases. Figure 45b shows the same region after straining to 0.4YS. No clear GB oxidization or crack initiation was observed except for some fine oxide particles. However, the distribution of these oxide particles was not uniform, forming conspicuous clusters and relatively large particles.

Figure 45c shows the same region after staining to 0.45YS. GBs become visible in secondary electron imaging mode due to oxidation, as indicated by the black arrows in Figure 45d. The oxidized GB above the triple junction (TJ) was decorated with dark regions, which are clearer in Figure 45f, as indicated by the black arrows. However, no such dark regions were observed below the TJ, which is clearer in Figure 45i. The EDS analysis (Figure 23) showed that the dark regions are rich in Cr and O indicating oxidation of the GB region. However, no crack initiated at GBs at this stress level. Figure 45e shows the surface morphology after straining to 0.5YS. The GB became more obvious and the visible length also increased from ~30 μm to ~80 μm. A careful look at the GB in the oxide cluster region revealed a small IG crack (Figure 45f), which evolved from the oxidized GB 0.45YS, whereas, the GB (below the TJ) with no obvious oxidation was still intact. Statistical analysis of all the cracks revealed that the majority of them were oxidized before cracking, although the exact initiation sites were not determined. The correlation of IG cracking with prior oxidation provides an indication of which boundaries are likely to crack upon further straining.

The basic process of GB oxidation is considered to occur by Fe dissolution and O internal diffusion along GB, to form Fe depletion and Cr-rich oxide on GB. When Fe dissolves into water, vacancies are formed and they diffuse along GB. In high-temperature primary water with hydrogen, Ni is thermodynamically stable. Therefore, it is considered that Cr preferentially forms oxides and that a part of Ni diffuses ahead of the GB oxide with vacancies to form Ni enrichment. On the other hand, Cr diffuses from the non-oxidized GB region to the GB oxide to mitigate the vacancy concentration gradient. It is considered the GB oxidation may be promoted by GB composition changes due to RIS. Fe and Cr depletion, and Ni and Si enrichment on GB were occurred due to RIS. It is known that Cr enhances corrosion resistance and Ni has higher oxidation potential. Experiments on proton irradiated 304 stainless steel [25] have revealed grain boundary migration near the surface, producing a region between the migrated and original grain boundaries that is Ni rich and Cr poor, caused by diffusion of Cr up the grain boundary to create the surface oxide. This phenomenon has been observed in Ni-base alloys 600 [26] and 690 [27]. It is not clear whether such a process enhances or suppresses the initiation of an IG crack along the grain boundary.

Si is an active element for oxidation, even more active than Cr [28]. SiO_2 is normally a protective oxide on Si-bearing alloys in a high-temperature gaseous environment. However, recent work has shown that this oxide is subject to dissolution in high-temperature water [29]. Consistently, Han et al. [30] reported that the oxide film formed on a model alloy containing 4.5 wt.% Si in simulated PWR primary water was porous and depleted in Si. The decreasing strength of the oxide film in the high Si model alloy reported by Li et al. [31] may be related to a compromised oxide structure. Therefore, the oxide on GB will be easily broken at the place where local stress is higher than the critical stress.
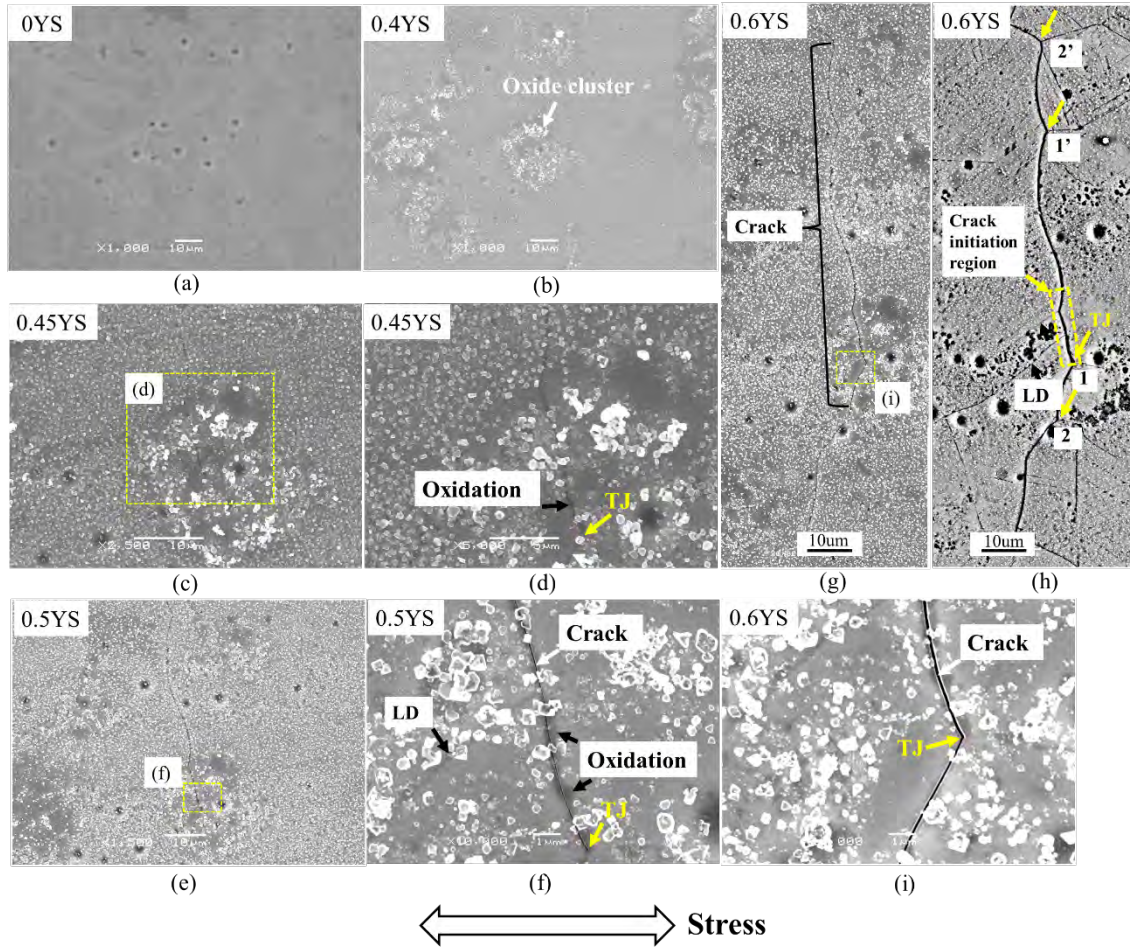
Figure 45. The initiation and propagation of a crack in B35-B1with the increase of stress and exposure time. (a) The surface morphology before exposure to high-temperature water; (b) Oxide particles formed after straining to 0.4YS. Some oxide particles were redistributed, forming clusters; (c-d) GB was oxidized after straining to 0.45YS; (e-f) Crack initiated at TJ and LD sites after straining to 0.5YS; (g-h) Crack propagated in the direction relatively normal to the direction of applied stress after staining to 0.6YS. (h) BSE image of the crack. (i) Crack at higher magnification.

The crack in Figure 45f revealed two micro-features that are likely correlated with crack initiation. One is the localized deformation (LD) structure indicated by a black arrow and the other one is the TJ indicated by a yellow arrow. If the localized deformation was a dislocation channel (DC), the concentrated stress at the DC-GB intersecting site could lead to cracking of an oxidized GB [5, 13, 14, 32]. As regards the TJ, the local stress at TJ can reach about twice the macroscopic stress due to the deformation constraint caused by adjacent grains, which could induce channeling, higher stress concentration, and consequently crack initiation. Another example of the occurrence of these micro-features along with a crack is provided in Figure 46. In this figure, both dark regions and very prominent localized deformation (channels) appeared at the crack initiation sites.
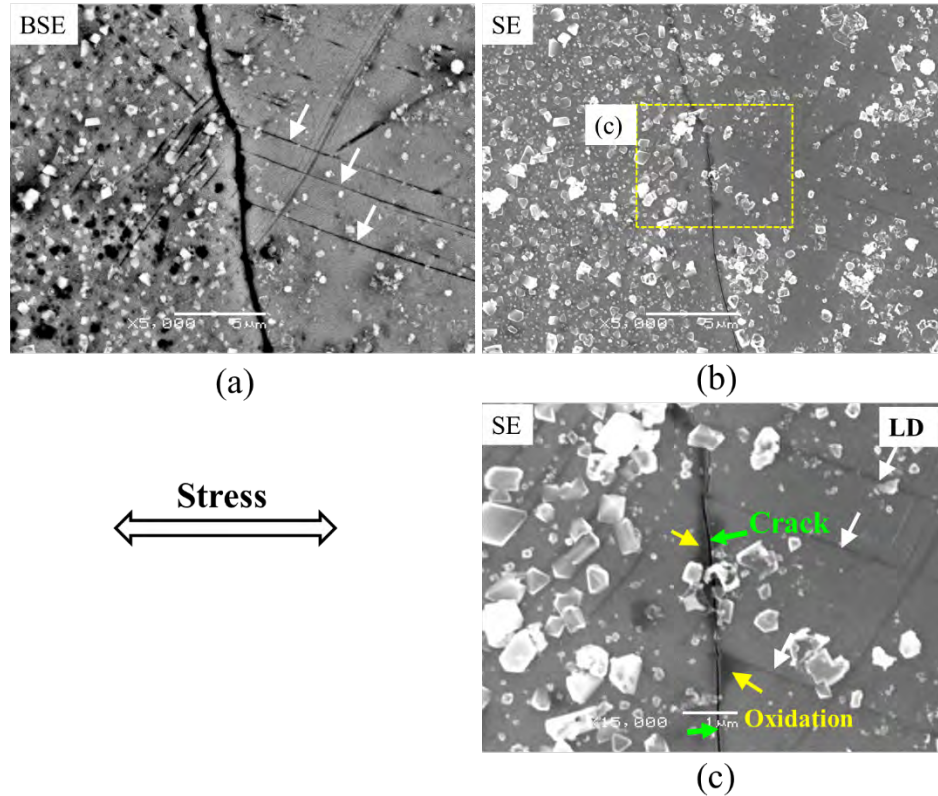
Figure 46. A representative crack from sample B35-B1 at 0.6YS. (a) BSE image (b) SE image of the same region, (c) magnified picture of the crack initiation sites.

Figure 45g shows the morphology after straining to 0.6YS. The short crack (~20 μm) at 0.5YS developed into a long crack (~90 μm) and the crack width also increased from ~ 80 nm to ~150 nm (Figure 45i). Figure 45h shows the same region but under BSE mode that better reveals microstructure features that were not clear in the SE image, such as GBs, TJs, and LDs. From this image, it was determined that the crack propagated from the initiation region in two directions (Figure 45h). The crack grew upwards and through the first TJ (1') and then propagated along the GB that has a large intersection angle (trace inclination) with the loading axis. After that, it stopped at the second TJ (2'), where both GBs have small trace inclinations. It also propagated down and through the TJ (1) and continued along the GB with a large trace inclination, finally stopping at the second TJ (2). Though the GB oriented nearly perpendicular to loading axis did not crack, it showed heavier oxidization than the one oriented nearly parallel to the loading axis

4.2.2   SA 304 SS

Recent studies of the crack initiation in irradiated austenitic stainless steels have shown an increasing relevance of the role of localized deformation in the IASCC susceptibility and crack initiation [5, 14, 33]. These studies have shown that grain boundaries that are intersected by discontinuous channel have a higher incidence of crack initiation compared to boundaries that transmit strain between adjacent grains [34, 35], and this enhanced cracking fraction is likely due to the high tensile stress at these intersections [35, 36].

This increase in stress has been linked to the pile-up of dislocations at the grain boundary after moving through the dislocation channel. The same is true for triple junctions, at which constraint by the adjacent grains results in a high local stress state.

In all three conditions, the cracks were found to initiate at very low stresses (low fractions of the yield stress) as shown in Figure 47. Crack initiation was found to always be preceded or accompanied by the activation of dislocation channels in the material as with the oxidization as the precondition. Upon further straining, the cracks were found to initiate at dislocation channel-grain boundary intersections. GB oxidization was found to occur in the environment and likely results in a decrease of GB strength. The degraded GB combined with the intersection of a dislocation channel with the GB is believed to be the reason for crack initiation at these sites. Figure 48 shows the change of full width at half maximum (FWHM) in an oxidized GB, a suspected crack, and a crack of different dpa samples. The suspected crack and crack have comparable width, however, the FWHM of oxidized GB is always smaller, indicating that cracks develop from oxidized GB.
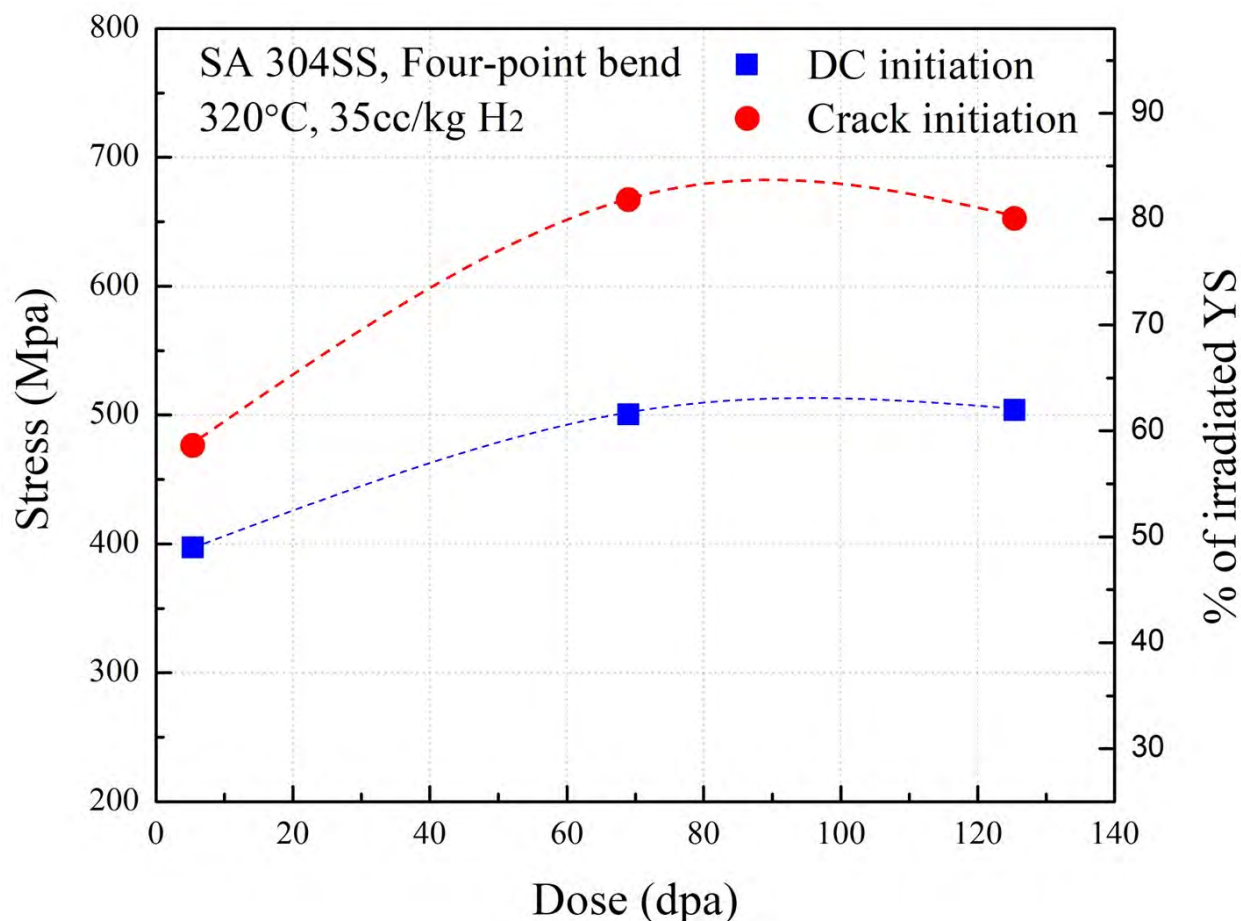
Figure 47. The stress required to cause formation of dislocation channeling and crack initiation in commercial purity SA 304 SS as a function of damage level.
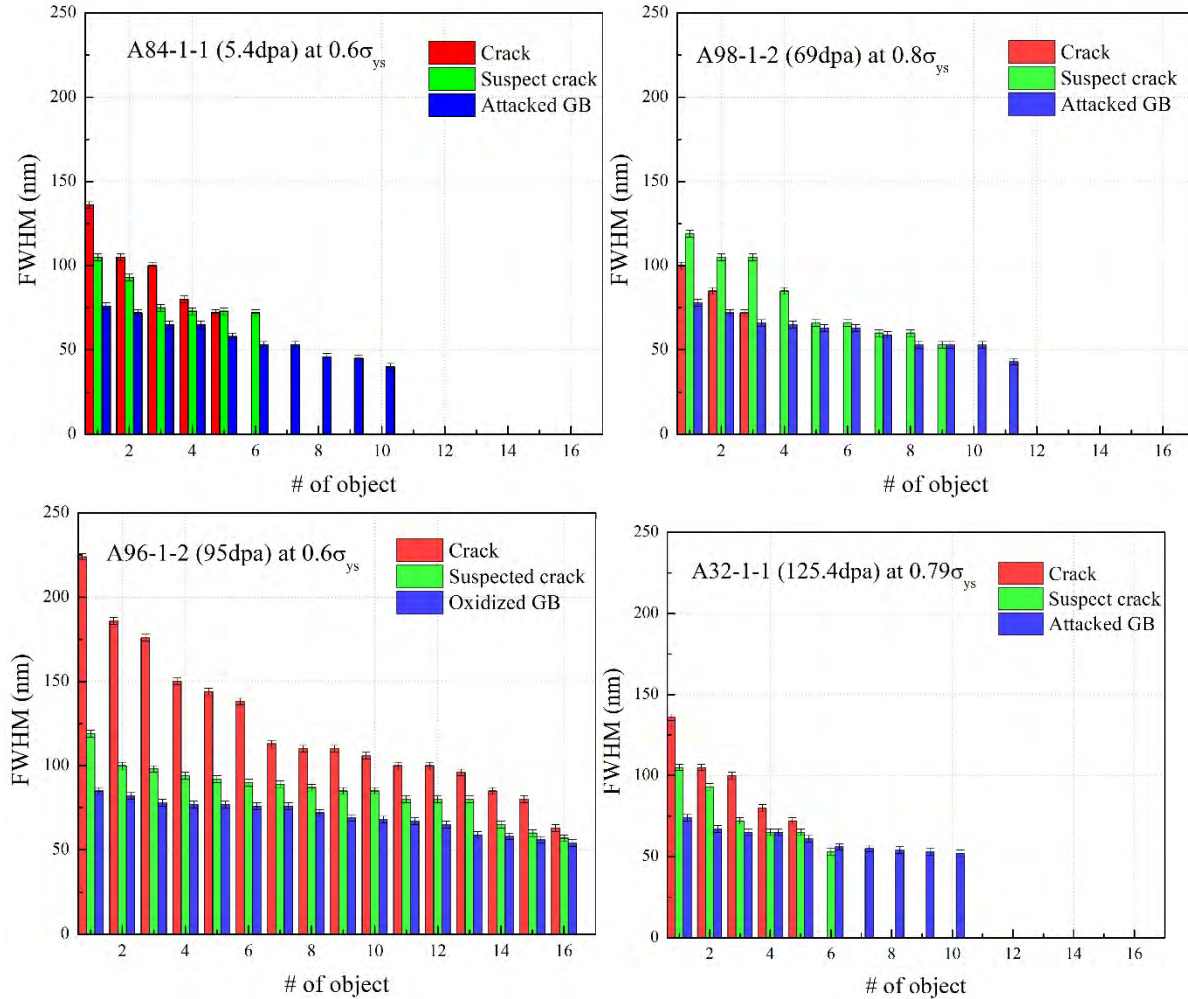
Figure 48. FWHM of oxidized GB, suspect crack and crack in different dpa samples.

4.3   IASCC Stress threshold

A stress threshold below which no IASCC crack initiation can occur was proposed [37] by summarizing the crack initiation data into a stress vs. dpa plot. This is a semi-empirical sensitivity criterion for crack initiation. With the increased data, the threshold value has dropped from 62% of the irradiated yield strength [37]to 50%[38, 39], to 40% [40, 41], and even 35% [42]. However, it is not clear whether this value will drop or not with additional data generated at higher dpa and on the testing to the much longer exposure time.

The stress required for crack initiation in CW 316 SS was found to be in the range of 0.4 - 0.5YS with only small variations with dose. Several cracks initiated in B101-B1 and B89-B1 at 0.5YS. However, only one crack initiated in B35-B1 at 0.45YS but the number increased quickly to 15 at 0.5YS, which is of the same order as B101-B1 and B89-B1. Considering the change of crack number with stress, it is possible to back extrapolate that the stress to initiate a crack in B101-B1 and B89-B1 may also be close to 0.45YS. As for SA 304 SS, the minimum to initiate a crack is at 0.6YS, which is higher than CW 316 SS. Though the

reason for this phenomenon is unknown. The preexisting slip bands and twins might be accountable for this. As these localized deformations might provide higher stress at the GB compared to the material without them.

With the four-point bend sample results obtained in this work, the applied stress as a percentage of the irradiated yield strength is plotted in Figure 49 as a function of dose along with available literature data [38-40, 42]. The closed symbols represent failure, while the open symbols represent non-failure. All the data are from PWR primary water relevant environments with small differences in testing temperature and water chemistry. Most all of the data were generated on C-ring and O-ring, and tensile samples under constant load with compression and tension, respectively. Usually, both types of tests are performed until the specimens fail, and the time to failure is associated with the time to initiation. This evaluation of initiation time can be considered satisfactory because the stressed part of the specimen has usually a small cross section in which the dimensions are associated with the initiation characteristic length considering an industrial criterion. The majority of the data is on CW 316 SS with a small amount on SA 304 SS. Despite differences in the shape of the sample and test method, the data from this study were consistent with the literature data.

From this figure, the minimum stress to initiate a crack in neutron-irradiated austenitic materials up to 125.4 dpa could be determined as 40% of their irradiated yield strength, as indicated by the dashed line. The closed symbol below the dashed line was not taken into account because this point was obtained in water with a very high concentration of Li (8 ppm). One drawback of this plot is that it does not incorporate the exposure time, as long exposure could result in cracking of samples designated as non-failure. Also, the irradiation condition (the neutron energy spectrum) of the sample was not considered. The thermal neutron spectrum can lead to a higher density of He bubbles in materials than the fast neutron spectrum at higher doses[43]. He bubbles existing on GBs have been reported by several researchers [12, 43, 44]. The bubbles on GBs could potentially enhance the IG embrittlement. Therefore, more data obtained from materials irradiated in thermal reactors under longer testing time and lower stress are in need.
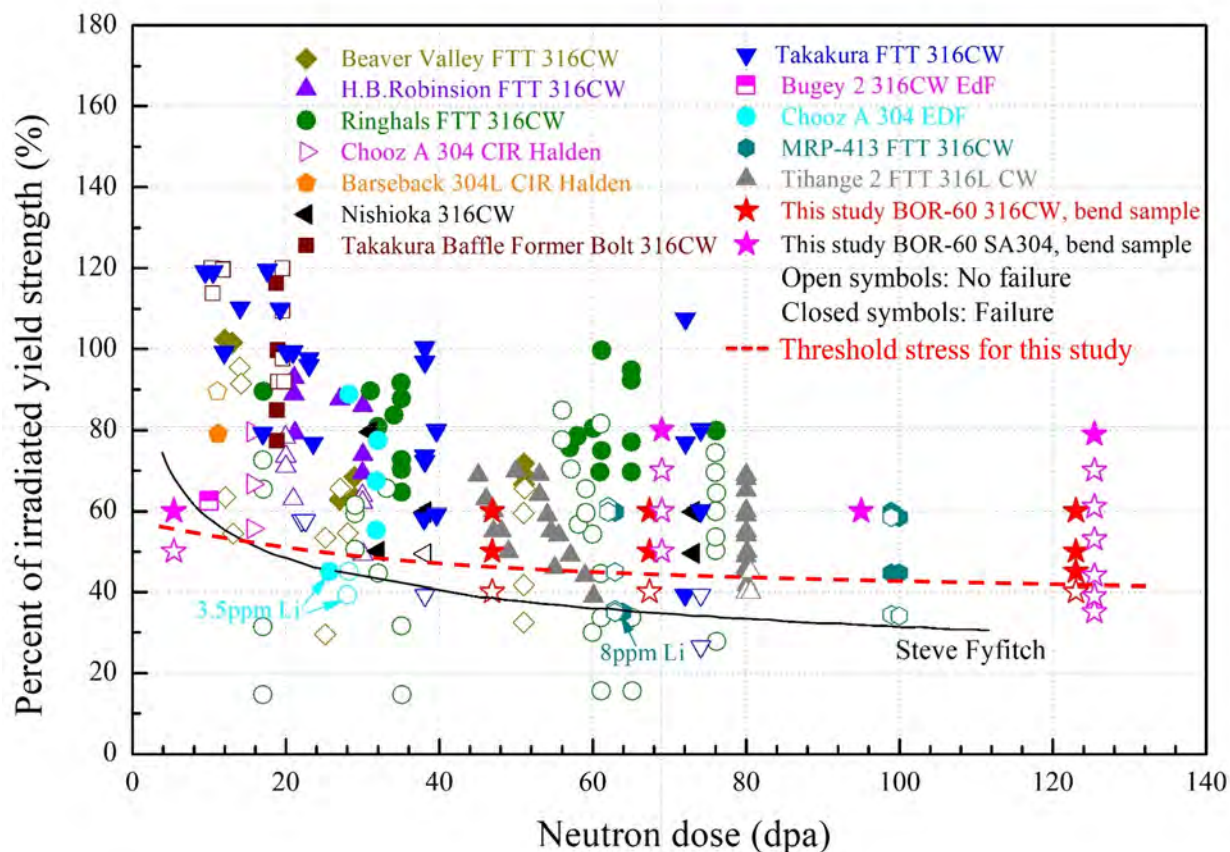
Figure 49. Stress as a percent of irradiated yield strength vs. neutron dose for IASCC crack initiation in austenitic stainless steels in a PWR primary water environment [38-40, 42]. Data for 304 and 316 in this study are offset along the abcissa to avoid overlap.

5.   CONCLUSION

Constant extension rate tensile studies using a single strain method on neutron irradiated CW316 stainless steel showed no dependence of IASCC on dose in the range of 46.9-125.4 dpa when measured by %IG on the fracture surface. SA304 stainless steel samples showed a slight but continuous increase in IASCC susceptibility with dose from 5.4 dpa to 125.4 dpa.

The mode of straining (interrupted vs. single strain or varying strain rates) had a significant influence on the resulting %IG of the fracture surface. The effect of strain mode on %IG in 316 is understood by normalizing the %IG to the exposure time after yielding. The %IG exhibited an inverse relationship with the time after yielding irrespective of the strain mode and dose of the sample.

Four-point bend tests were conducted to correlate the crack initiation behavior with localized deformation. The advantage of these tests is that the growth of cracks is suppressed due to the increasingly compressive stress field normal to the surface. These tests were highly successful in catching crack shortly after initiation, identifying the threshold stress for crack initiation, and linking them to the microstructure.

Cracks formed at stresses as low as 45% of the irradiated YS in CW 316 SS and 60% of the irradiated YS in SA 304 SS.

Severe GB oxidization was observed before crack initiation, indicating that GB oxidization may be a precursor to crack initiation. Additional features that are linked to crack initiation are localized deformation and triple junctions. Cracks always nucleated at the grain boundary where at least one adjacent grain exhibited heavy localized deformation (DCs, slip lines, twins) or at triple junction where the local stress was also large. Most of the initiated cracks had a trace inclination larger than 50° and they also propagated along GBs having a larger trace inclination, indicating the normal stress dependence of crack initiation and propagation.

Based on these results and a comparison with literature data, an apparent IASCC stress threshold was determined as 40% of the irradiated yield strength for the neutron-irradiated SS up to a dose of 125.4 dpa with minimal dependence on dose beyond about 5 dpa.

References

[1] EPRI. CIR II Program: Description of the Boris 6 and 7 Experiments in the BOR-60 Fast Breeder Reactor. (2005).

[2] EPRI. Materials reliability program: A review of the cooperative irradiation assisted stress corrosion cracking research program (MRP-98). EPRI Report, vol. 10028072003.

[3] T. Malis, S.C. Cheng, R.F. Egerton. EELS log-ratio technique for specimen-thickness measurement in the TEM. J Electron Microsc Tech. 8 (1988), 193-200.

[4] D.J. Edwards, E.P. Simonen, S.M. Bruemmer. Evolution of fine-scale defects in stainless steels neutron-irradiated at 275 °C. J NUCL MATER. 317 (2003), 13-31.

[5] K.J. Stephenson, G.S. Was. The role of dislocation channeling in IASCC initiation of neutron irradiated stainless steel. J NUCL MATER. 481 (2016), 214-225.

[6] K.J. Stephenson. The role of dislocation channeling in IASCC initiation of neutron irradiated austenitic stainless steel [Ann Arbor: University of Michigan; 2016.

[7] G.W. HOLLENBERG, G.R. TERWILLIGER, R.S. GORDON. Calculation of Stresses and Strains in Four-Point Bending Creep Tests. J AM CERAM SOC. 54 (1971), 196-199.

[8] S.R. W. Critical analysis of "tight cracks". CORROS REV. 28 (2010), 1-103.

[9] A. Renault, C. Pokor, J. Garnier, J. Malaplate. Microstructure and grain boundary chemistry evolution in austenitic stainless steels irradiated in the BOR-60 reactor up to 120 dpa. Conf. on Environmental Degradation of Materials in Nuclear Power Systems, Virginia Beach, VA, 2009. pp. 1324-1334.

[10] D.J. Edwards, E.P. Simonen, F.A. Garner, L.R. Greenwood, B.M. Oliver, S.M. Bruemmer. Influence of irradiation temperature and dose gradients on the microstructural evolution in neutron-irradiated 316SS. J NUCL MATER. 317 (2003), 32-45.

[11] K. Fukuya, K. Fujii, H. Nishioka, Y. Kitsunai. Evolution of microstructure and microchemistry in cold-worked 316 stainless steels under PWR irradiation. J NUCL SCI TECHNOL. 43 (2006), 159-173.

[12] M. Song, K.G. Field, R.M. Cox, G.S. Was. Microstructural characterization of cold-worked 316 stainless steel flux thimble tubes irradiated up to 100 dpa in a commercial Pressurized Water Reactor. J NUCL MATER. 541 (2020), 152400.

[13] J. Hesterberg, Z. Jiao, G.S. Was. Effects of post-irradiation annealing on the IASCC susceptibility of neutron-irradiated 304L stainless steel. J NUCL MATER. 526 (2019), 151755.

[14] Z. Jiao, G.S. Was. Localized deformation and IASCC initiation in austenitic stainless steels. J NUCL MATER. 382 (2008), 203-209.

[15] E.A. West, G.S. Was. Strain incompatibilities and their role in intergranular cracking of irradiated 316L stainless steel. J NUCL MATER. 441 (2013), 623-632.

[16] M.D. McMurtrey, G.S. Was, L. Patrick, D. Farkas. Relationship between localized strain and irradiation assisted stress corrosion cracking in an austenitic alloy. Materials Science and Engineering: A. 528 (2011), 3730-3740.

[17] M. Kamaya, Y. Kawamura, T. Kitamura. Three-dimensional local stress analysis on grain boundaries in polycrystalline material. INT J SOLIDS STRUCT. 44 (2007), 3267-3277.

[18] E.A. West, G.S. Was. IGSCC of grain boundary engineered 316L and 690 in supercritical water. J NUCL MATER. 392 (2009), 264-271.

[19] T. Fujii, K. Tohgo, Y. Mori, Y. Miura, Y. Shimamura. Crystallographic and mechanical investigation of intergranular stress corrosion crack initiation in austenitic stainless steel. Materials Science and Engineering: A. 751 (2019), 160-170.

[20] M.N. Gussev, J.T. Busby. Deformation localization in highly irradiated austenitic stainless steels. Oak Ridge National Lab2014.

[21] Z. Jiao, J. Hesterberg, G.S. Was. Insights into the sources of irradiation hardening in a neutron irradiated 304L stainless steel following post-irradiation annealing. J NUCL MATER. 526 (2019), 151754.

[22] T. Toyama, Y. Nozawa, W. Van Renterghem, Y. Matsukawa, M. Hatakeyama, Y. Nagai, A. Al Mazouzi, S. Van Dyck. Irradiation-induced precipitates in a neutron irradiated 304 stainless steel studied by three-dimensional atom probe. J NUCL MATER. 418 (2011), 62-68.

[23] K. Fukuya, H. Nishioka, K. Fujii, T. Miura, Y. Kitsunai. Local strain distribution near grain boundaries under tensile stresses in highly irradiated SUS316 stainless steel. J NUCL MATER. 432 (2013), 67-71.

[24] T. Fukumura, K. Fukuya, K. Fujii, T. Miura, Y. Kitsunai. Grain boundary oxidation of neutron irradiated stainless steels in simulated PWR water. Proceedings of the 18th International Conference on Environmental Degradation of Materials in Nuclear Power Systems – Water Reactors. Springer, Boston, MA, 2019. pp. 2153-2163.

[25] M. He, D.C. Johnson, G.S. Was, I.M. Robertson. The role of grain boundary microchemistry in irradiation-assisted stress corrosion cracking of a Fe-13Cr-15Ni alloy. ACTA MATER. 138 (2017), 61-71.

[26] L. Volpe, M.G. Burke, F. Scenini. Understanding the role of Diffusion Induced Grain Boundary Migration on the preferential intergranular oxidation behaviour of Alloy 600 via advanced microstructural characterization. ACTA MATER. 175 (2019), 238-249.

[27] W. Kuang, M. Song, G.S. Was. Insights into the stress corrosion cracking of solution annealed alloy 690 in simulated pressurized water reactor primary water under dynamic straining. ACTA MATER. 151 (2018), 321-333.

[28] W. Kuang, J. Hesterberg, G.S. Was. The effect of post-irradiation annealing on the stress corrosion crack growth rate of neutron-irradiated 304L stainless steel in boiling water reactor environment. CORROS SCI. 161 (2019), 108183.

[29] K.A. Terrani, Y. Yang, Y.J. Kim, R. Rebak, H.M. Meyer, T.J. Gerczak. Hydrothermal corrosion of SiC in LWR coolant environments in the absence of irradiation. J NUCL MATER. 465 (2015), 488-498.

[30] G. Han, Z. Lu, X. Ru, J. Chen, J. Zhang, T. Shoji. Properties of oxide films formed on 316L SS and model alloys with modified Ni, Cr and Si contents in high temperature water. CORROS SCI. 106 (2016), 157-171.

[31] G.F. Li, Y. Kaneshima, T. Shoji. Effects of Impurities on Environmentally Assisted Crack Growth of Solution-Annealed Austenitic Steels in Primary Water at 325°C. CORROSION-US. 56 (2000), 460-469.

[32] K. Fukuya. Current understanding of radiation-induced degradation in light water reactor structural materials. J NUCL SCI TECHNOL. 50 (2013), 213-254.

[33] Z. Jiao, G.S. Was. Impact of localized deformation on IASCC in austenitic stainless steels. J NUCL MATER. 408 (2011), 246-256.

[34] M.D. McMurtrey, B. Cui, I. Robertson, D. Farkas, G.S. Was. Mechanism of dislocation channel-induced irradiation assisted stress corrosion crack initiation in austenitic stainless steel. Current Opinion in Solid State and Materials Science. 19 (2015), 305-314.

[35] D.C. Johnson, B. Kuhr, D. Farkas, G.S. Was. Quantitative linkage between the stress at dislocation channel – Grain boundary interaction sites and irradiation assisted stress corrosion crack initiation. ACTA MATER. 170 (2019), 166-175.

[36] D.C. Johnson, B. Kuhr, D. Farkas, G.S. Was. Quantitative analysis of localized stresses in irradiated stainless steels using high resolution electron backscatter diffraction and molecular dynamics modeling. SCRIPTA MATER. 116 (2016), 87-90.

[37] P.D. Freyer, T.R. Mager, M.A. Burke. Hot cell crack initiation testing of various heats of highly irradiated 316 stainless steel components obtained from three commercial PWRs. Proc. of 13th Int. Conf. on Environmental Degradation of Materials in Nuclear Power Systems-Water Reactors, Whistler, British Columbia, 2007.

[38] O.K. Chopra, A.S. Rao. A review of irradiation effects on LWR core internal materials – IASCC susceptibility and crack growth rates of austenitic stainless steels. J NUCL MATER. 409 (2011), 235-256.

[39] C. Pokor, J.P. Massoud, M. Wintergerst, A. Toivonen, U. Ehrnstén, W. Karlsen. Determination of the time to failure curve as a function of stress for a highly irradiated AISI 304 stainless steel after constant load tests in simulated PWR water environment. Fontevraud 7: Contribution of Materials Investigation to Improve the Safety and Performance of LWRs, Avignon, France, 2010.

[40] R.W. Bosch, M. Vankeerberghen, R. Gérard, F. Somville. Crack initiation testing of thimble tube material under PWR conditions to determine a stress threshold for IASCC. J NUCL MATER. 461 (2015), 112-121.

[41] K. Takakura, K. Nakata, K. Fujimoto, K. Sakima, N. Kubo. IASCC properties of cold worked 316 stainless steel in PWR primary water. Proc. of 14th Int. Conf. on Environmental Degradation of Materials in Nuclear Power Systems2009. pp. 1207-1218.

[42] S. Fyfitch, S. Davidsaver, K. Amberge. Irradiation-assisted stress corrosion cracking initiation screening criteria for stainless steels in PWR systems. Proceedings of the 18th International Conference on Environmental Degradation of Materials in Nuclear Power Systems – Water Reactors. Springer2017. pp. 995-1004.

[43] K. Fujimoto, T. Yonezawa, E. Wachi, Y. Yamaguchi, M. Nakano, R.P. Shogan, J.P. Massoud, T.R. Mager. Effect of the accelerated irradiation and hydrogen/helium gas on IASCC characteristics for highly irradiated austenitic stainless steels. In: T.R. Allen, P.J. King, L. Nelson, 编者. (Eds.). Proceedings of the 12th International Conference on Environmental Degradation of Materials in Nuclear Power System – Water Reactors. TMS2005. pp. 299-310.

[44] D. Edwards, E. Simonen, S. Bruemmer. Microstructural evolution in neutron-irradiated stainless steels: Comparison of LWR and fast-reactor irradiations. Proceedings of 12th International Conference on Environmental Degradation of Materials in Nuclear Power Systems – Water Reactors2005. pp. 419-428.